Report No. **D1.3.2**	
Title of Report:	**Material properties as a function of environmental and operational conditions**

Mohamed Saleh (TUD) Prakash Venkatesan (TUD) Sina Askarinejad (CAM) Ioannis Katsivalis (CAM)	Sofia Teixeira De Freitas (TUD) Wim De Waele (UGent)	1	31/03/2020
Written by: (Name, Signature)	Verified by : (Name, Signature)	Revision	Date

EXECUTIVE SUMMARY

This report is primarily focused on the characterization of the adhesive material's, mechanical and moisture resistance, properties and the interface characterization of bi-material (steel to CFRP) adhesively-bonded joint. The adhesive used in this research is a Methylacrylate-based (MMA) adhesive. For the long-term performance investigation, an ageing campaign for the bulk adhesive is designed. Salt spray ageing conditions are applied as detailed later in this report. In addition, the interface properties are evaluated in the non-aged state and 6 weeks-aged state to determine the effect of the moisture and salt water on the joints' properties, via fracture toughness mode I and mode II tests. In addition, investigation of water transport into the bulk MMA adhesive using three different techniques – a) classical gravimetric technique b) Electrochemical impedance spectroscopy and c) using Fourier Transform Infrared Attenuated Total Reflection (FTIR–ATR) is implemented. The methods are used to quantitatively determine the diffusion coefficient as well as the maximal water absorption to the bulk adhesive. Furthermore, the effect of temperature in combination with water uptake is also investigated. Besides, the effect of water ingress on the steel-adhesive interface stability is probed using scanning kelvin probe (SKP) technique. The SKP provides important insight into the interfacial delamination mechanisms and the rate of delamination. The combined results from these different techniques provide key information about the role played by moisture in degradation of the adhesive as well as in debonding behavior at the steel-adhesive interface.

TABLE OF CONTENTS

LIST OF FIGURES

LIST OF TABLES

1. INTRODUCTION

The use of adhesively-bonded joints in maritime applications is still limited nowadays. One of the main reasons for this limited application is the level of knowledge and engineering data available being scarce. Lack of such data hinders the maritime industry from being able to predict the structural integrity and life expectancy (≥ 25 years) of adhesively-bonded joints especially when exposed to the marine harsh environment. Key elements in the design process include: the deep understanding of the load transfer mechanisms in such joints, the long-term performance of adhesively-bonded joints, their failure mechanisms, and the degradation due to the environmental conditions. The availability of standardized test methods, generating these engineering data and quantifying the joints' properties, provides the designers and manufacturers with the essential confidence level to put their designs forward into application. Generally, testing can be divided into two main categories: i) determining the material properties of the bulk adhesive, which helps in the adhesive selection process and ii) determining the quality and response of the bonded joint, which supports the design process of the joint.

Moreover, one of the limiting factors preventing widespread use of adhesively bonded joints in marine environment is the degradation of the bonded joints through water ingress. Water ingress can occur either through bulk diffusion into the adhesive or along the interfacial region between the adhesive and the adherend. The effects of degradation might also be accelerated in the presence of other factors such as elevated temperature or mechanical stress. The properties of bulk adhesive can be influenced by water uptake resulting in swelling, plasticization or in leaching some of the components in the adhesive. On the other hand, water ingress along the interface can also adversely affect the interfacial bonding resulting in the delamination of the adhesive from the adherend or in the corrosion of the metal substrate.

This report is primarily focused on the characterization of the adhesive material's, mechanical and moisture resistance, properties and the interface characterization of bi-material (Steel to CFRP) adhesively-bonded joint. The adhesive used in this research is a Methacrylate-based (MMA) adhesive. For the long-term performance investigation, an ageing campaign for the bulk adhesive is designed. Salt spray ageing conditions are applied as detailed later in this report. In addition, the interface properties are evaluated in the non-aged state and 6 weeks-aged state to determine the effect of the moisture and salt water on the joints' properties, if any. In addition, this report comprises an investigation of water transport into the bulk MMA adhesive using three

different techniques – a) classical gravimetric technique b) Electrochemical impedance spectroscopy and c) using Fourier Transform Infrared Attenuated Total Reflection (FTIR–ATR). The methods were used to quantitatively determine the diffusion coefficient as well as the maximal water absorption to the bulk adhesive. Furthermore, the effect of temperature in combination with water uptake was also investigated. Besides, the effect of water ingress on the steel-adhesive interface stability is probed using Scanning Kelvin Probe (SKP) technique. The SKP provides important insight into the interfacial delamination mechanisms and the rate of delamination. The combined results from these different techniques provide key information about the role played by moisture in degradation of the adhesive as well as in debonding behavior at the steel-adhesive interface.

1.1. Bulk adhesive characterization

1.1.1. Tensile dog-bone specimens

One of the main advantages of testing the bulk adhesive in tension is the fact that the specimen's geometry, being dog-bone shaped, results in an area of a uniform stress state. In this sense, the resultant stress can be directly related to the applied force as function of the specimen's cross-sectional area. Moreover, this specific geometry ensures the final failure happens in the gauge section away from the gripping region where stress concentrations occur. Figure 1 depicts a typical stress-strain curve of adhesive materials with the linear elastic and non-linear regions. The stiffness/modulus, yield stress, strain-to-failure and ultimate tensile strength can be determined accordingly. The tensile modulus and Poisson's ratio are generally calculated over the range of strains 0.05% to 0.25 % as per the testing standards' guidelines.

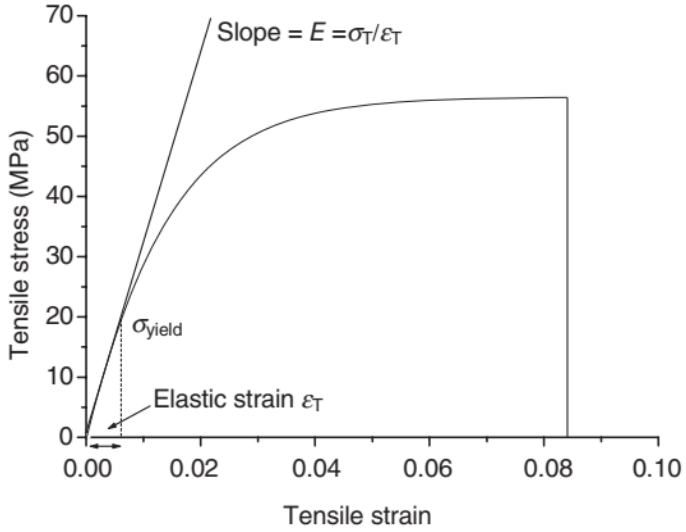

Figure 1 A typical tensile stress-strain curve for adhesives [1]

The effect of the marine environment on the mechanical properties of the bulk adhesive is, thus, quantified via examining the degradation of the stiffness, strength and strain-to-failure of the bulk adhesive. The bulk adhesive specimens are exposed to salt spray ageing as discussed later in Section 2.1.1.

1.1.2. Moisture uptake

Electrochemical Impedance Spectroscopy measurements

Electrochemical impedance spectroscopy (EIS) is a non-destructive technique in which a sinusoidal voltage is applied to measure the current response. A typical EIS measurement consists of an electrochemical cell with three electrodes (working, reference and counter electrodes) and a potentiostat equipped with frequency response analyzer is used to determine the impedance of the system (Figure 2).

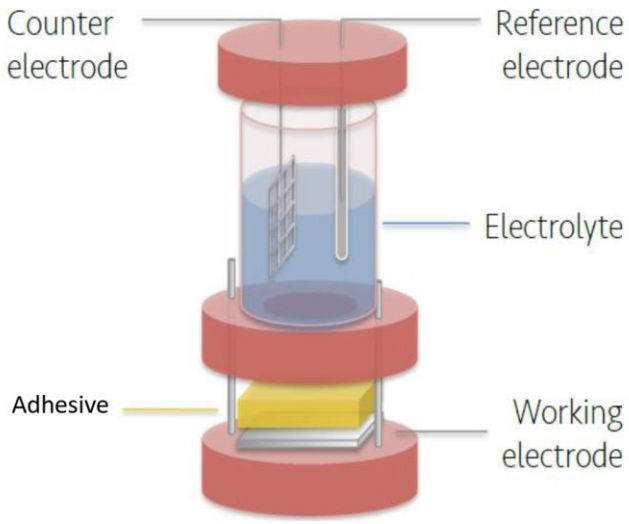

Figure 2 Illustration of the electrochemical cell used in EIS experiments

When the water percolates into the adhesive coated over the top of the substrate, it increases the permittivity of the adhesive. This dielectric constant of a typical polymeric material (usually about 3–8) is markedly different from that of water (78.5 at 25 °C) [2]. Thus, during water uptake the effective dielectric constant increases which in turn results in the increase of capacitance of the adhesive. Thus, by monitoring capacitance over time, EIS serves as an effective tool to study the water uptake kinetics and thereby to determine the percentage of water in the adhesive as well as the diffusion coefficient of water.

The capacitance of the adhesive is given by the equation

$$C = \frac{1}{2\pi f Z_i} \quad (1)$$

where Z_i is the imaginary part of the impedance at the excitation frequency f. The objective of EIS measurement is to provide comparable data to the classical gravimetric water uptake measurement and at the same time compare water uptake in a free film and a supported adhesive over metal.

Fourier Transform Infrared Attenuated Total Reflection (FTIR–ATR) spectroscopy

FTIR is a technique which can provide information about the functional groups present in the molecule. The absorption of IR light with characteristic wavenumber is correlated to a transition between discrete vibration states and typically wavenumbers between 400 cm^{-1} and 4000 cm^{-1} are studied. The number of excitable vibrations is dependent on the geometry of a molecule.

In the ATR configuration, a crystal with high refractive index (ZnSe, Ge) is used and under certain angles of incidence the incident beam is entirely reflected if the medium in contact with the crystal has lower refractive index. This allows in-situ monitoring of the change in sample composition and one of the applications has been to monitor the water absorption in organic coatings and adhesives.

In this study, ATR-FTIR is used as a spectroscopic tool to provide complimentary data to the water uptake curves obtained using gravimetric and EIS studies. The water uptake can be monitored by observing the increase in absorbance of the bulk water and hydroxyl peaks over time and Fieldson-Barbari equation can be used to calculate the diffusion coefficient. Additionally, ATR-FTIR also offers the possibility to deconvolute the peaks which can provide information about the different water bands (clustered, monomeric, dimeric and bulk water) which in turn can provide insights about the state of water at different times of absorption.

1.2. Interface characterization

As highlighted in the introduction, the second category of testing is concerned with the quality and response of the bonded joint to the external loads. These external loads can be in the form of mechanical or hygrothermal loads which may lead to crack initiation and propagation in service. Such crack propagation can occur either in the adhesive, the adherend or at the adhesive/adherend interface [3]. Failure due to crack propagation can be speeded up further by

the harsh environmental conditions in maritime applications [4] such as moisture and corrosion. In addition, it can happen under different modes of loading as depicted in Fig. 3. Normally the crack propagation occurs due to mixed-mode conditions in real life applications. However, testing individual modes is essential to obtain the engineering data required for the characterization of the bonded joints and for the interfacial properties, which is then used as an input for the simulation and predictive purposes. Thus in this research work, the mode I and mode II fracture toughness for the adhesively-bonded joints are investigated. To take into account the degradation effect due to the environmental conditions, non-aged specimens are compared with 6 weeks-aged specimens while keeping all the other geometrical parameters the same.

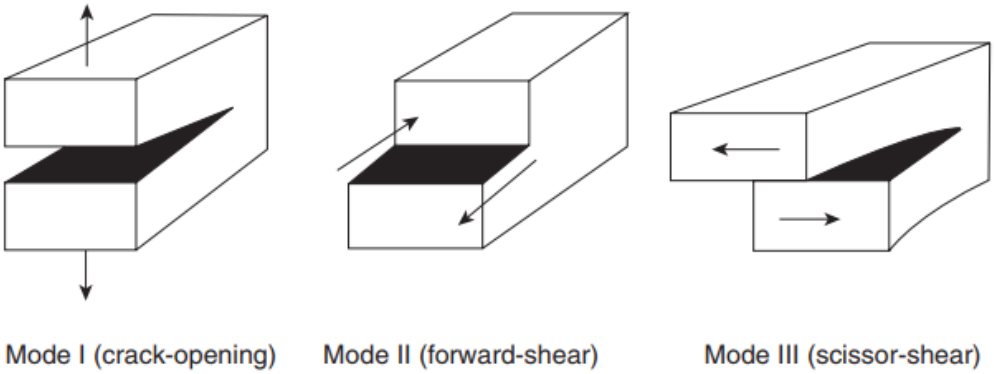

Figure 3 A schematic of the different modes of fracture [1]

1.2.1. Mode I fracture toughness

The most commonly used testing to determine the initiation and propagation fracture toughness (G_I) under the opening mode I is the double cantilever beam (DCB) test. This test is carried out by applying a normal displacement to the crack plane with an initial pre-cracking length (a_o) as shown in the schematic in Fig. 4. Crack length is then monitored during the test and correlated to the load and displacement values to calculate the initiation and propagation fracture toughness. Fabrication and testing of DCB specimens is straightforward and can be easily implemented by a standard testing machine. The test guidelines, procedure, specimens preparation and data reduction are detailed in ASTM D5528 standard [5]. Another under-development technique is introduced, by University of Cambridge, in the Appendix as the 90° peel test.

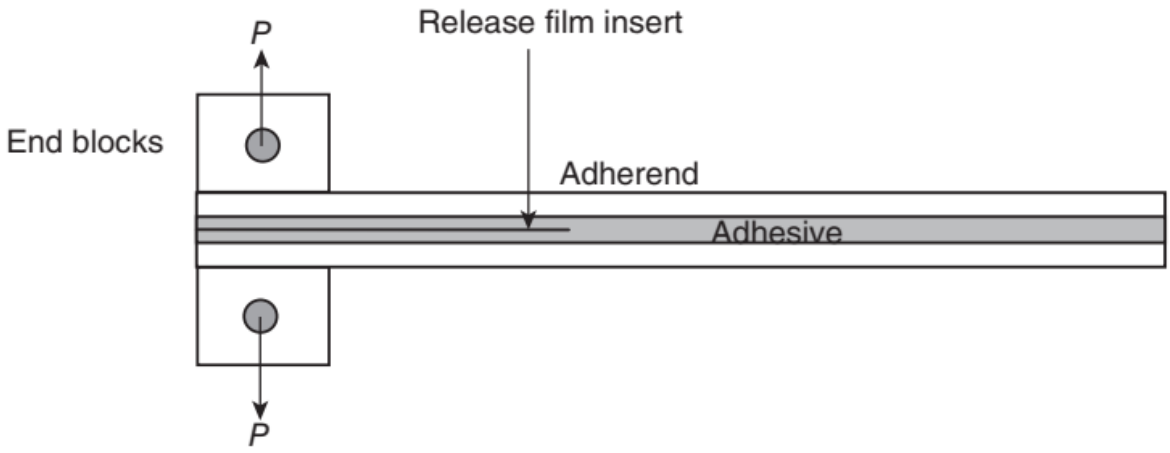

Figure 4 A schematic of DCB testing [1]

1.2.2. Mode II fracture toughness

Shear is a common loading scenario for adhesives in bonded structures. However, the fracture mechanism of adhesive layers with thicker bondlines under mode II loading is still unclear. Polymeric materials, like adhesives, display pressure-sensitivity [6] and therefore have different response depending on the type of loading [7]. Therefore, studying with independent tests the responses in modes I and II is important.

Shear loading can be introduced in adhesives by torsional and tensile shear. Torsional shear tests include tests on bulk specimens, butt joints [8] and the napkin ring test (ASTM E 229). However, these tests require the introduction of twisting and measuring the resulting rotational motion which requires specialized equipment and is not straightforward. In comparison tensile shear tests include: the Iosipescu [9] and the Arcan [10] tests, the single and double-lap shear tests [11], and the Thick Adherend Shear Test (TAST) [12].

The single lap joint geometry inherently causes an eccentricity in the applied load path, leading to out-of-plane bending moments and subsequently elevated peel stresses. This is particularly important in joints containing composite adherends due to their low strength in the through-thickness direction. Hence, these peel stresses can lead to premature failure of the joint. The problem of eccentricity in loading, is solved in double-lap shear tests and thick-adherend shear tests.

Based on the advantages mentioned above, the thick-adherend shear test was selected as the methodology for the extraction of the degraded properties after exposure to salt-water and elevated temperatures under mode II loading.

1.2.3. Delamination crack-growth

Scanning Kelvin Probe – Delamination measurement

Scanning Kelvin Probe (SKP) is an important technique that is used to investigate buried polymer/oxide/metal interfaces. It is a non-destructive vibrating capacitor technique which measures the contact potential difference between a vibrating probe and a conductive sample. The needle tip, sample surface and the air in between (dielectric) forms a parallel plate capacitor and any changes in sample surface due to water/ion ingress or structural rearrangement will cause a change in the charging condition of the capacitor. When an external electric contact, between two surfaces, is made, the Fermi levels equalize and periodic modulation of distance between two electrodes induces a flow of current in the external circuit of SKP which is then translated into a change in Volta potential (Figure 5A).

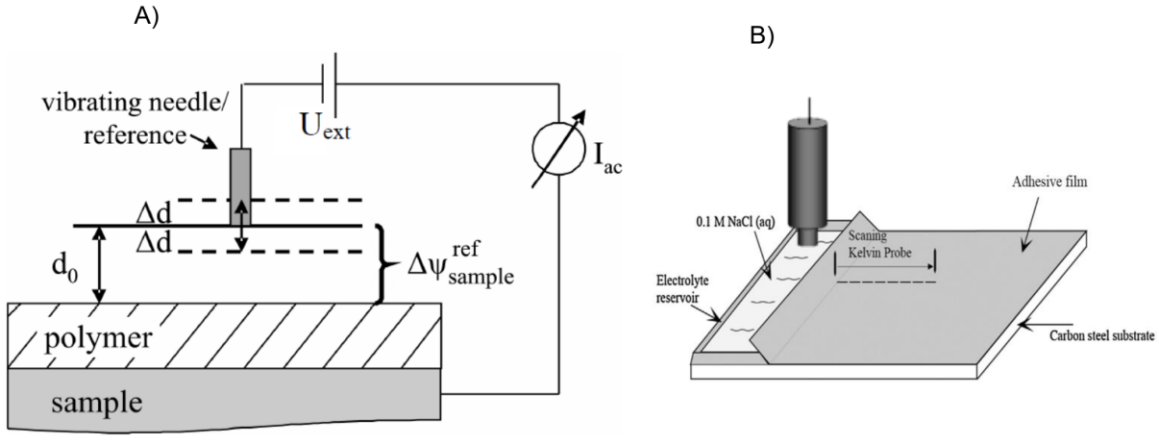

Figure 5 Principles of a Kelvin Probe: A) set up and B) Schematic illustration of a typical delamination measurement [13]

The objective of this measurement is to investigate the delamination of the adhesive from the metal in an open configuration (Figure 5B). A defect region is created for the electrolyte reservoir and the probe measures the intact region over time to probe the buried interface to measure delamination kinetics.

2. EXPERIMENTAL PROCEDURE

2.1. Bulk adhesive characterization

2.1.1. Tensile dog-bone specimens

For the tensile testing characterization of the adhesive, the ASTM D638 procedure is followed. The adhesive plates were manufactured by injection using a pneumatic gun with a mixing ratio

of 10:1 by volume. All manufactured plates were room temperature cured for 24 hours then post cured at 80°C for 1 hour. Afterwards, these plates were water-jet cut to the desired dog-bone shape. The dimensions of the dog-bone specimens are depicted in Fig. 6. The nominal thickness of the specimens was ~ 2.6 mm. In order to investigate the effect of the environmental and operational conditions on the material properties of the bulk adhesive, batches of at least 5 specimens are tested on a weekly basis for the first 4 weeks. This interval is increased to bi-weekly from the 4th week to the 8th week. Finally, one last batch of specimens is tested at the 14th week. The weight of these batches is monitored throughout the testing campaign to determine the saturation level and correlate it to the mechanical response. The conditions for the ageing in the salt-spray chamber is set according to the ASTM B117 [14]. These conditions are 5% salinity, 35°C and 50% humidity.

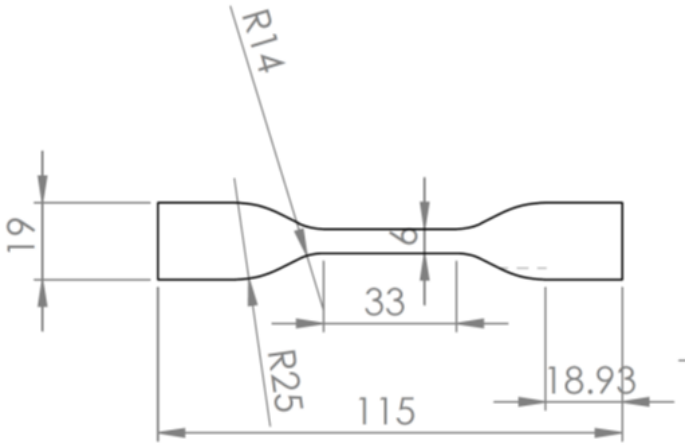

Figure 6 Dimensions of the tensile dog-bone specimen in mm

The test was carried out using displacement-controlled mode, with a displacement rate of 1.27 mm/min. This rate was kept constant throughout the testing campaign as well as the initial scoping testing in the project to avoid any strain-rate effect on the results. The machine used for testing was a Zwick Roell machine equipped with a 10 kN load cell and hydraulic grips to minimize the slippage due to gripping. In addition, Digital Image Correlation (DIC) was used to capture the displacement and deformation of the specimen during testing (see Fig. 7).

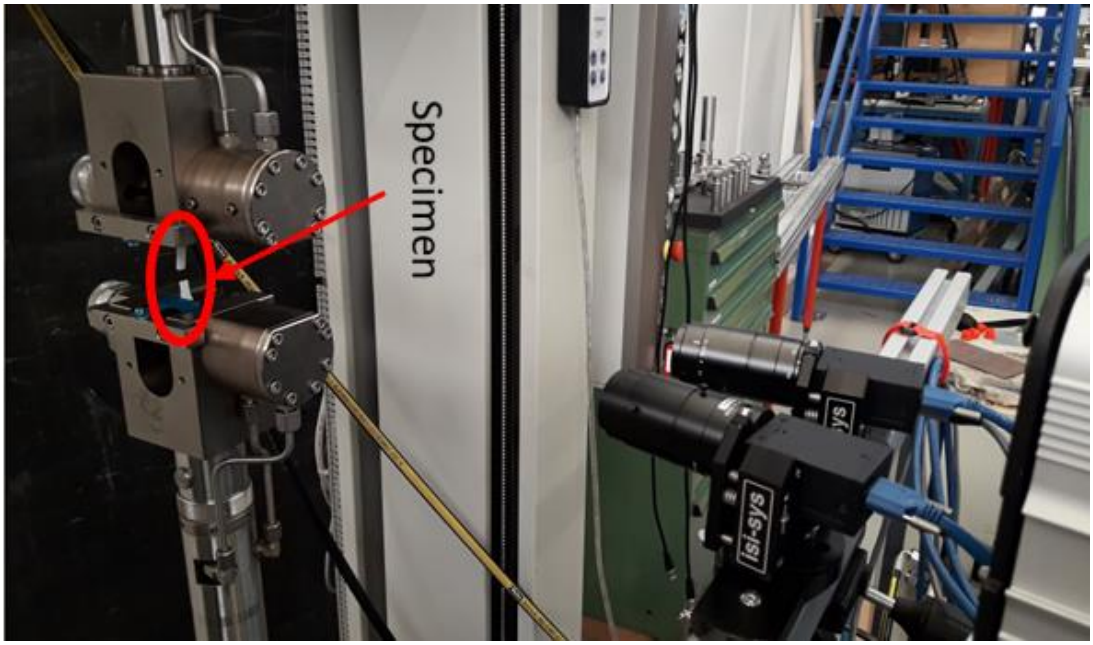

Figure 7 Tensile dog-bone testing setup (the specimen shown is after testing)

2.1.2. Moisture uptake

Gravimetric measurements

Free standing MMA adhesive films for gravimetric measurements were prepared by pressing the adhesive between two plexiglass plates covered on the pressing side with a mylar releasing film. After 24 hours of curing, circular discs of diameter 18 mm or 20 mm were cut out. Films of two different thicknesses (710 ± 20 µm or 420 ± 30 µm) were prepared. The water uptake was measured in both electrolyte (3.5 % NaCl) and in deionized water. A microbalance - Mettler Toledo XSR 105- was used with an accuracy of 0.01 mg. At least 3 samples were measured for each condition. Besides room temperature measurement, high temperature measurements at 40 ^{o}C and 80 ^{o}C were also performed with a heating bath controlled by the heating liquid propylene glycol. After immersion, samples were periodically measured by quickly drying them within a minute.

EIS – Water Upake

The AH36 high strength steel was cut to a dimension of 35 mm x 35 mm. Before applying the adhesive, the steel was abraded with an automated grinding machine (Struers Rotopol 31/Rotoforce 4, Struers A/S) with rotation speed of 150 rpm and a sample rotation speed of 40 rpm at a pressure of 0.5 MPa. The samples were abraded with abrasive SiC paper up to 2000-grit followed by polishing with diamond suspension paste of 3 µm and 1 µm particles.

Then the samples were ultrasonically cleaned with isopropanol and dried with compressed air. The adhesive was applied and smoothened with a metallic rod after which it was pressed with a plexiglass covered with mylar tape to mitigate void/bubble formation. The adhesive was left to cure at room temperature for 24 hours. A three-electrode electrochemical cell with a Ag/AgCl (3M KCl) reference electrode and a stainless steel mesh counter electrode was used. The steel coated with adhesive was used as the working electrode with 1 cm^2 exposed area of the adhesive. For the high temperature experiment, the sample was immersed in the beaker and a heating plate was used with constant monitoring of temperature. A Bio-logic potentiostat SP200 was used to measure the impedance by sweeping the frequency of the AC perturbation signal from 0.1 to 10 mHz. The amplitude of the AC excitation voltage was 10 mV.

ATR-FTIR – Water Uptake

ATR-FTIR (Thermo Nicolet Nexus FTIR) with mercury-cadmium-telluride as a liquid nitrogen cooled detector was used with a Veemax III single reflection ATR accessory to study the transport of IR active species into the adhesive. Germanium internal reflection elements (PIKE Technologies) were used with a fixed face angle of 60°. The spectra were collected in the region of 4000–600 cm^{-1} at a resolution of 8 cm^{-1} and 1000 scans per spectrum. The spectrum is collected in absorbance format, $-\log (R/R_0)$, where R and R_0 are the reflectance from sample and background respectively. OMNIC 8.1 software package (ThermoElectron Corporation, Madison, WI) was used to obtain the spectra.

For the water uptake measurement, the adhesive was coated over Ge IRE crystal with a thickness of 180 ± 30 µm and cured for 24 hours. Importantly, the spectra of the adhesive coated crystal was taken and used as the background. For high temperature measurements (40 ^oC and 80 ^oC), the crystal was mounted on a cell which had a temperature stage and the temperature was controlled with a software.

2.2. Interface characterization

To fully characterize the interface, the fracture toughness due to opening (mode I) and in-plane shear (mode II) were considered. In addition, the delamination crack growth rate is studied. Based on initial testing [3,15], it was concluded that the weak interface is the adhesive/steel interface. Moreover, due to salt spray ageing this interface is expected to experience more degradation due to the corrosion of the steel. Thus, this testing campaign is focused only on this interface, not the composite/adhesive interface. The latter will be investigated later in the project to support the simulation by the material/interfaces inputs.

2.2.1. Mode I fracture toughness

As the objective of the study is to investigate the steel/adhesive interface, a Teflon film/insert was placed at one of the two interfaces prior to injecting the adhesive for the bonding. In other words, the specimen (see Fig. 8) consists of two rectangular steel plates bonded together by Methyl-Methacrylate (MMA) adhesive with a nominal thickness of 8 mm. A non-adhering Teflon tape film was placed at the interface between adhesive and one of the steel plates to obtain a discontinuity in the bond line which represented an initial crack of length a_0 = 50mm as shown in Figure 9. As no pre-cracking was carried out, the crack tip is referred to here as a notch which might have an effect on the DCB testing as it will be shown later in this report. Moreover, some voids are observed in the specimens as highlighted in Fig. 8.

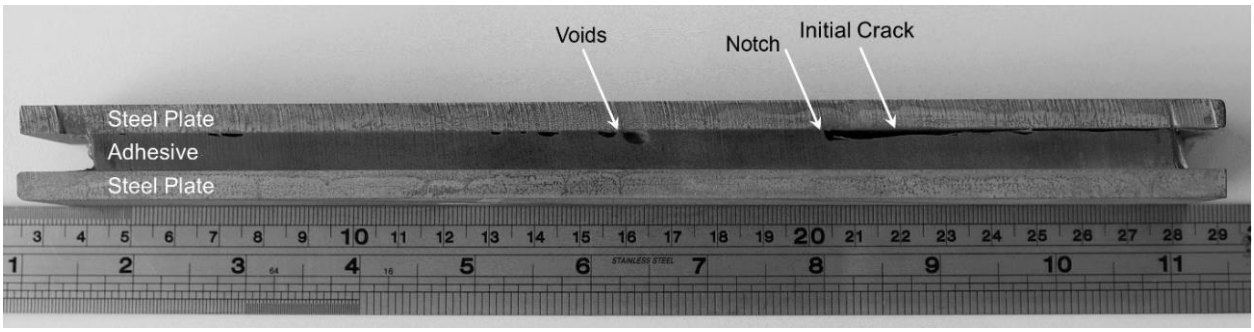

Figure 8: Double cantilever beam specimen with a discontinuity at the adhesive-steel interface

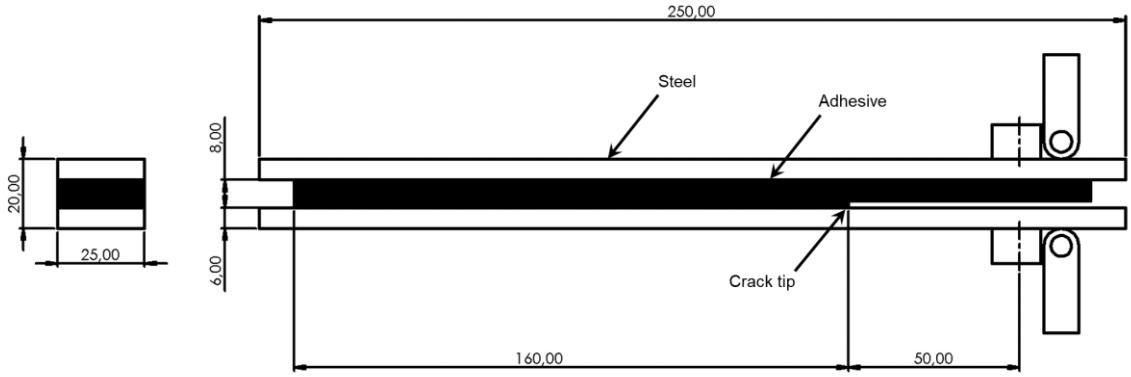

Figure 9: Dimensions of the DCB specimen used for the testing

As the adhesive bond-line is relatively thick (~ 8mm) and the pre-crack is introduced at one of the adhesive-substrate interfaces, this leads to asymmetric specimen configuration. This directly had an effect on the fracture toughness mode in question. Thus, virtual crack closure technique (VCCT) was used to simulate the specimen using ABAQUS Standard. The model was used to simulate the steel-to-steel bonded DCB specimen with a bond-line thickness of 8 mm and steel

thickness of 6 mm. The initial crack length was set to 50 mm, and the boundary conditions were specified to resemble the DCB testing boundary conditions by having a displacement applied at the upper loading pin and allowing only rotation around the centerline of the lower pin. The model was meshed with element type C3D8R: A 8-node linear brick, reduced integration, hourglass control element, resulting in approximately 150k nodes for 125k elements. Figure 10 shows the energy release rate distribution for both mode I and mode II along the width of the specimen at the crack tip. It is clear that the geometrical asymmetry resulted in a dominant Mode I (~90 %) rather than having a pure Mode I.

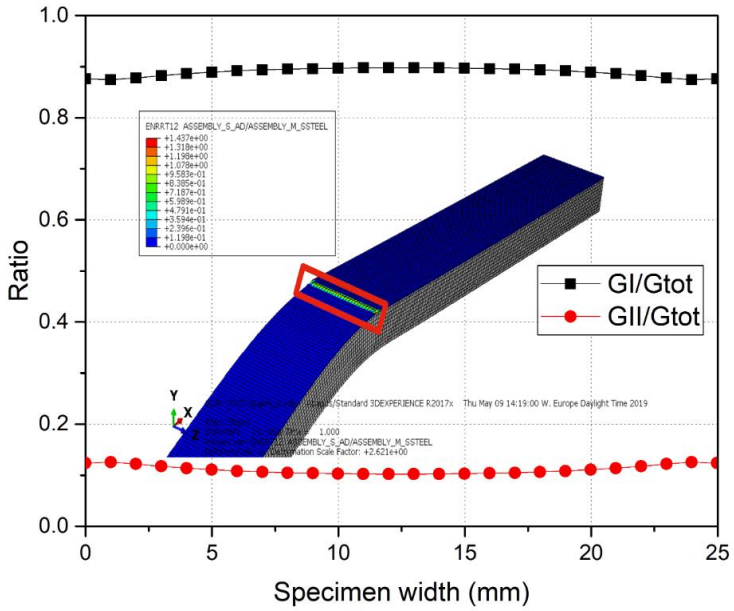

Figure 10 The energy release rate ratio across the DCB specimen's width

The test setup for both quasi-static and fatigue testing is identical. As per the ASTM D5528 standard, the test was carried out using displacement-controlled mode, with a displacement rate of 1.27 mm/min. This rate was kept constant throughout the testing campaign as well as the initial scoping testing in the project to avoid any strain-rate effect on the results. The machine used for testing was a Zwick Roell machine equipped with a 10 kN load cell. In addition, DIC was used to capture the displacement, strain distribution ahead of the crack tip and the crack growth. The DIC system was synchronized with the mechanical testing machine via analogue connections. Figure 11 demonstrates the test setup used for the DCB testing. It is worth mentioning here that unlike the dog-bone tensile testing campaign, the DCB test was carried out for only 2 cases: the non-aged case vs. 6-weeks of salt spray ageing.

Figure 11 DCB testing setup

2.2.2. Mode II fracture toughness

There are many different types of Thick-Adherend-Shear-Test (TAST) specimens which are based on the work of Krieger [16]. The testing configuration has been studied extensively. Kassapoglou and Adelman [17] studied the effect of adhesive/substrate modulus mismatch on the adhesive shear distribution along the bond length and concluded that decreasing modulus mismatch significantly increases the non-uniformity of the shear stress distribution.

To evaluate the mechanical properties of the adhesive under shear and the adhesive/steel interface fracture properties, a modified TAST joint was designed and manufactured (see Fig. 12). Pre-cracks of length a_0 were placed at each end of the adhesive layer, as shown in Fig. 1. Specimens with selected adhesive layer thickness h = 3, 5, 8, 10, 13 mm, and pre-crack length a_0 = 0, 10, 20 mm were manufactured and tested. After investigating the effect of adhesive layer thickness and pre-crack length, the effect of aging was evaluated on specimens without a pre-crack. The effect of aging on pre-cracked specimens is assumed to be the same.

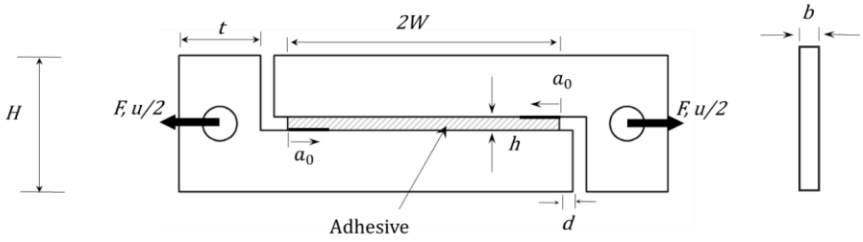

Figure 12: Sketch of the modified TAST joint (2W = 100 mm, h = 3, 5, 8, 10, 13 mm, H = 50.4 mm, t = 30 mm, a_0 = 0, 10, 20 mm, d = 5 mm, b = 6.35 mm)

The shear strength of a pre-cracked specimen is measured as a function of the adhesive layer thickness, h, and the pre-crack length, a_0. The aim of the study is to measure the fracture response of the joint including the degree of crack extension versus shear displacement across

the adhesive layer. Digital Image Correlation (DIC) was used to track the shear strains and crack extensions. Tests were conducted at room temperature on the TAST specimens by a screw-driven test bench (Instron 5500R-6025). The shear strain rate of $6 \times 10^{-4} s^{-1}$ was applied to the specimens, hence the machine cross-head speed was varied according to the adhesive thickness.

The failure mechanism of a typical TAST specimen is displayed in Figure 13, showing the typical load-displacement curve and the DIC images corresponding to different events. The load-displacement curve consists of a linear section, followed by a strain hardening section before reaching the final failure. The onset of cracking in the load-displacement curve is shown in point 2. From point 2 to 3, the two interfacial cracks propagate gradually while the load is increasing. At point 3, the load starts to gradually drop while the cracks start to propagate faster. By making use of the load-displacement curves and obtaining the net-section shear stresses $\tau_{net} = F/2b(W-a)$ and shear strains across the adhesive layer ($\bar{\gamma} = u/h$), the shear behavior of adhesive was deduced.

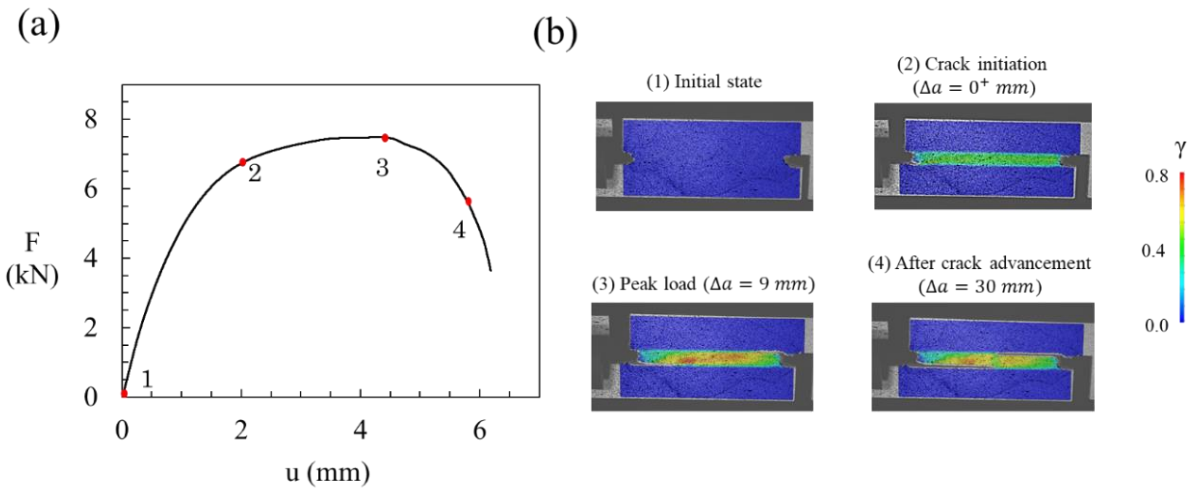

Figure 13: (a) Typical load-displacement curve of a TAST specimen with h=8 mm and a0 = 10 mm ($\dot{\gamma} = 6 \times 10^{-4}$), (b) Corresponding DIC image of each deformation stage

The magnitude of the critical separation was obtained using Digital Image Correlation (DIC). As it is schematically shown in Fig. 14a, five digital gauges were placed behind the crack tip and their deformation was traced. The distance between the gauges was 1 mm, and the first one was 1 mm far from the crack tip. Fig. 14b shows the horizontal displacement versus the distance from the crack tip for a representative case (h = 8 mm and a_0 = 20 mm) measured by the digital gauges. For this case, at the onset of cracking which happens at a shear strain

across the adhesive layer of $\bar{\gamma}$ = 0.33, the displacement jump between the adhesive and the substrate was 1.4 mm. These measurements were performed for various specimens and the average value of δ_c= 1.3 mm was obtained.

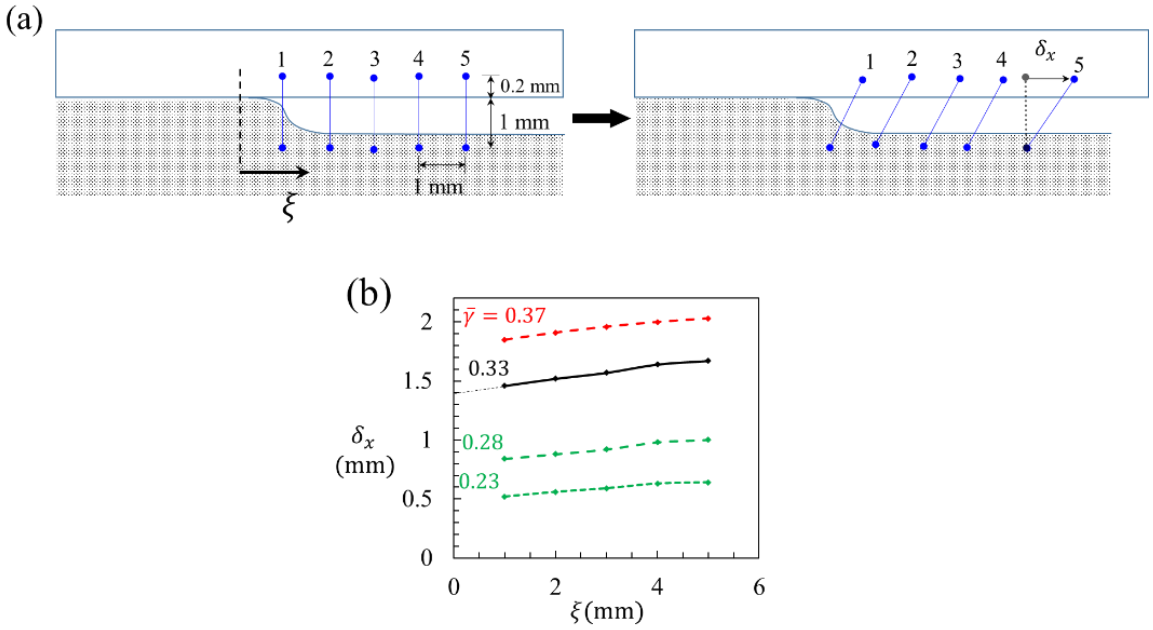

Figure 14: (a) Schematic of the method employed to obtain the displacement jump at the crack tip prior to crack growth. (b) A typical result obtained (h = 8 mm, a_0 = 20 mm), $\bar{\gamma}$ = 0.33 is the onset of cracking

2.2.3. Delamination crack-growth

SKP – Delamination

The steel was prepared in the same way as mentioned in the EIS section. A PTFE tape was then placed at the edge of the sample masking a partial area to create an artificial defect for electrolyte reservoir. On either side of the sample, adhesive tapes were pasted so that the thickness of the adhesive can be controlled to be 120 ± 10 µm. The adhesive was applied and smoothened with a metallic rod after which it was pressed with a plexiglass covered with mylar tape to mitigate void/bubble formation. The adhesive was left to cure at room temperature for 24 hours. After curing, the PTFE tape was lifted up creating a bare metal area. A reservoir was created using Permatex® 80022 silicone gasket which could then hold the electrolyte – 3.5 % NaCl solution.

The metal coated with was placed in the humidity chamber of the Kelvin probe instrument (SKP5050) for at least 16 hours and allowed to equilibrate at a relative humidity of 93%. After

equilibrating, 3.5 wt% of NaCl solution was added to the defect to initiate delamination. A Ni/Cr probe was used with a 500 μm circular flat end. The probe was scanned over the adhesive film from the defect towards the intact area.

3. RESULTS AND DISCUSSION

3.1. Bulk adhesive characterization

3.1.1. Tensile dog-bone specimens

Figure 15 summarizes the stress-strain response for the entire testing campaign. As shown in the figure, the testing campaign included: non-aged and intervals-aged specimens in weeks. The non-aged stress-strain curves demonstrate an elastic-plastic response with approximately 250 MPa tensile modulus, 10 MPa stress at failure and 36 % strain at failure. The main difference between the shipyard specimen and the rest is the manufacturing process. In the case of the shipyard specimen, no post-curing was carried out in order to resemble the actual environmental conditions of the joint manufacturing unlike the lab-controlled environment for the rest of the specimens.

In order to accurately quantify the effect of ageing on the mechanical response of the bulk adhesive, the moisture uptake (see Fig.17) was monitored for the dog-bone specimens. This should help in determining the state of saturation of the bulk adhesive through the weeks. Saturation of the bulk adhesive is observed starting from the 6th week ($\sqrt{}$time ~ 32$\sqrt{}$h) onwards with a moisture uptake percentage of ~ 1.2%.

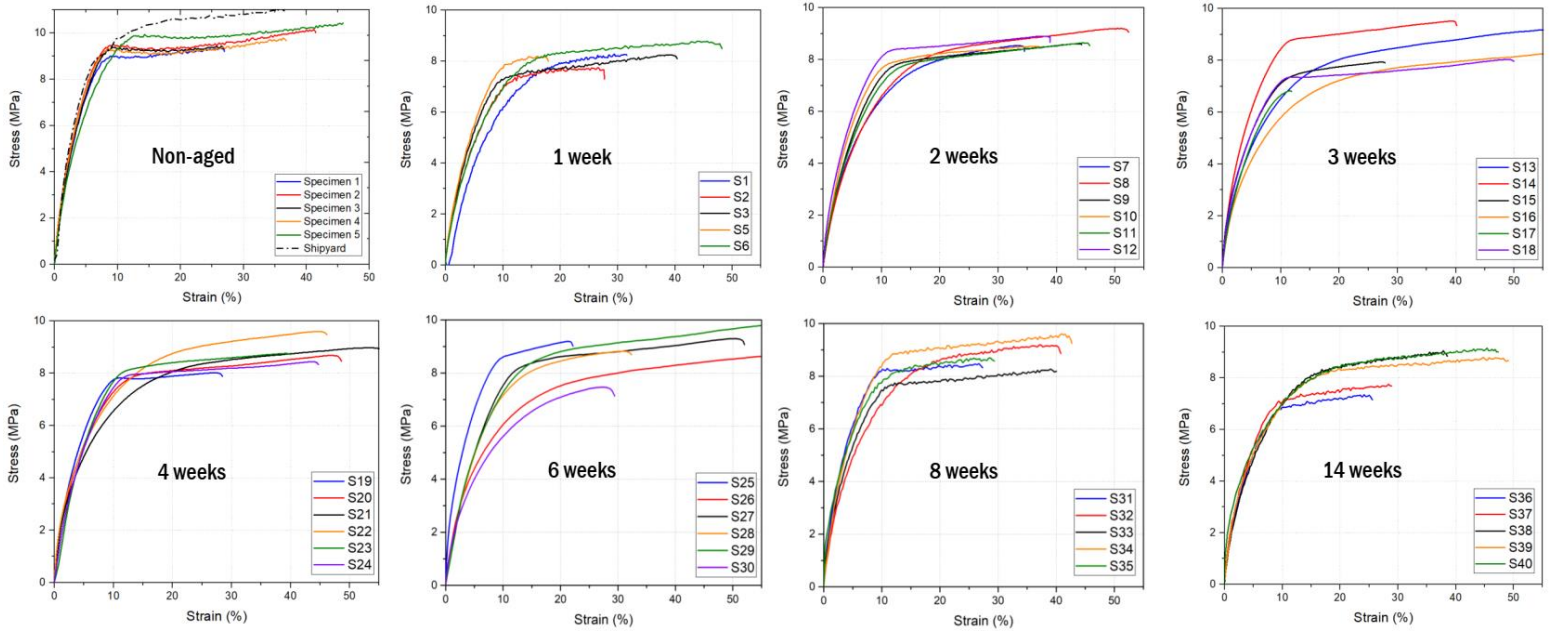

Figure 15 Summary of the stress-strain curves as function of the ageing duration in weeks

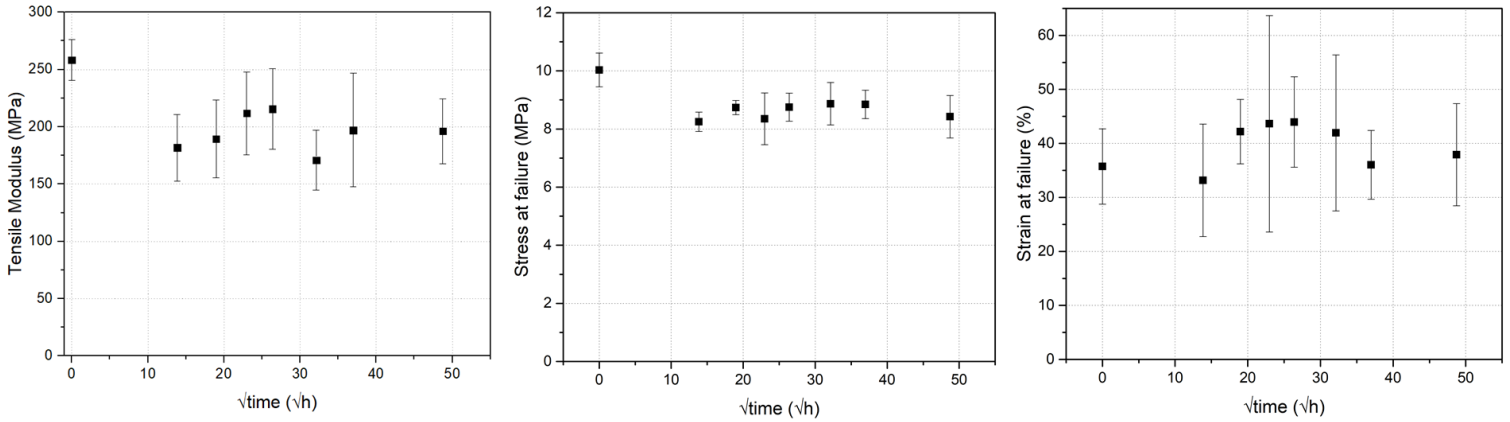

Figure 16 Summary of the (a) Tensile modulus, (b) Stress at failure, (c) Strain at failure as function of the ageing duration in √h

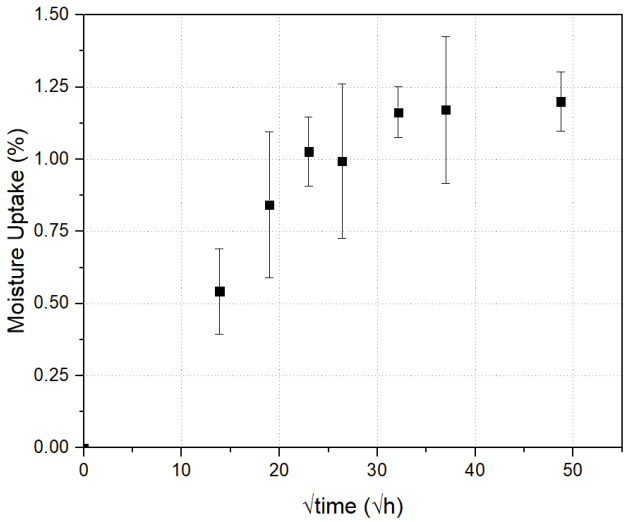

Figure 17 Moisture uptake as function of the ageing duration in √h

Although the adhesive does not experience saturation in the weeks 1 to 4, the effect on the mechanical response is captured by monitoring the tensile modulus and the stress at failure. Table 1 and Figure 16 summarize this effect of salt-spray ageing on the bulk adhesive. There is almost a 20 % reduction of both the tensile modulus and the strength at failure. Comparison of the modulus, strain and stress to failure clearly highlights the first reduction that occurs once moisture diffuses into the bulk adhesive. However, from this point till full saturation, the significance of ageing and moisture diffusion is almost minor. Even after reaching saturation (√h > 30), the change in the tensile modulus and the stress at failure is minimal. Moreover, the strain at failure (see Fig 16) experiences a higher level of scatter due to the variation within each single batch of specimens. These observations suggest that once the moisture diffuses into the bulk adhesive and even before full saturation, a reduction of approximately 20% is expected for the modulus and the strength. Afterwards, the effect of ageing on the bulk adhesive is less significant than the experimental scatter in a single batch being tested.

Table 1 Summary of the tensile dog-bone testing results

Time (√h)	Moisture Uptake (%)	Tensile Modulus (MPa)	Strain at failure (%)	Stress at failure (MPa)
0.00	0.00 ± 0.00	258.11 ± 17.83	35.73 ± 6.97	10.03 ± 0.58
13.86	0.54 ± 0.15	181.77 ± 28.97	33.17 ± 10.42	8.25 ± 0.33
18.97	0.84 ± 0.25	189.41 ± 33.81	42.17 ± 5.97	8.74 ± 0.24
22.98	1.03 ± 0.12	211.79 ± 36.19	43.63 ± 20.05	8.35 ± 0.89
26.38	0.99 ± 0.27	215.57 ± 35.02	43.95 ± 8.38	8.75 ± 0.48
32.12	1.16 ± 0.09	170.93 ± 26.28	41.95 ± 14.43	8.87 ± 0.73
36.99	1.17 ± 0.25	197.02 ± 49.53	36.04 ± 6.37	8.85 ± 0.49
48.74	1.20 ± 0.10	196.07 ± 28.22	37.90 ± 9.46	8.42 ± 0.73

3.1.2. Moisture uptake

Gravimetric – Water uptake

The gravimetric result for the free standing adhesive at room temperature in salt water solution is presented in Figure 18 .

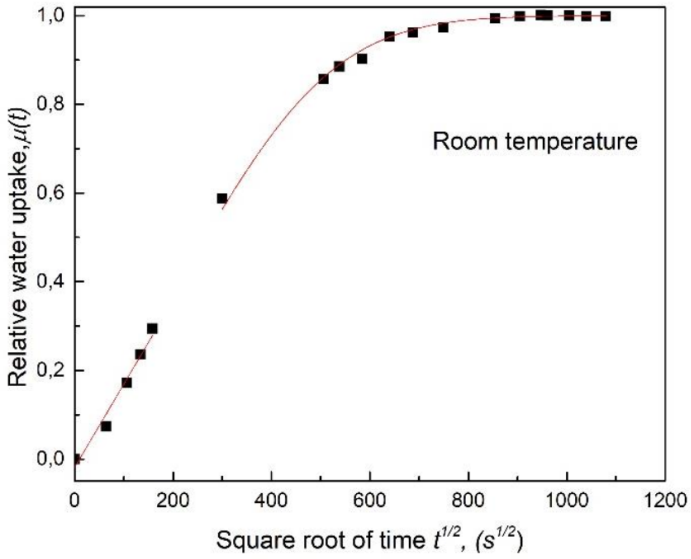

Figure 18 Relative water uptake μ(t), as a function of square root of immersion time at 25 ± 1 ^{o}C in 3.5% NaCl for circular adhesive (20 mm diameter & 720 ± 15 μm thickness)

The relative water uptake μ(t) is calculated from the equations [18]

$$\mu(t) = \frac{m_t - m_o}{m_{max} - m_o} \tag{2}$$

where m_t , m_o and m_{max} are polymer mass at time t, t = 0 and at final equilibrium. The diffusion coefficient is calculated from the relative water uptake by

$$\mu(t) = \frac{4}{\sqrt{\pi}}\frac{\sqrt{t}}{\sqrt{\tau}} \;; \mu(t) < 0.5 \tag{3}$$

$$\mu(t) = 1 - \frac{8}{\pi^2} e^{\pi^2 t/\tau} \;; \mu(t) > 0.5 \tag{4}$$

where $\tau = \frac{h}{D\beta^2}$ and $\beta = 1 + 2h/d$ and h is disc thickness, d is disc diameter, t is time, β is geometrical correction factor for edge effects. The maximal water absorption is given by

$$W = \frac{m_{max} - m_o}{m_o} \tag{5}$$

The water uptake curves obtained were linear in the beginning and thus met the criteria for being Fickian. Eventually they reached saturation within a few days. It is very important here to note that the experiments have been continued for more than nine months and the weight of the immersed adhesive has remained constant. The diffusion coefficient and maximal water absorption are tabulated in table 2.

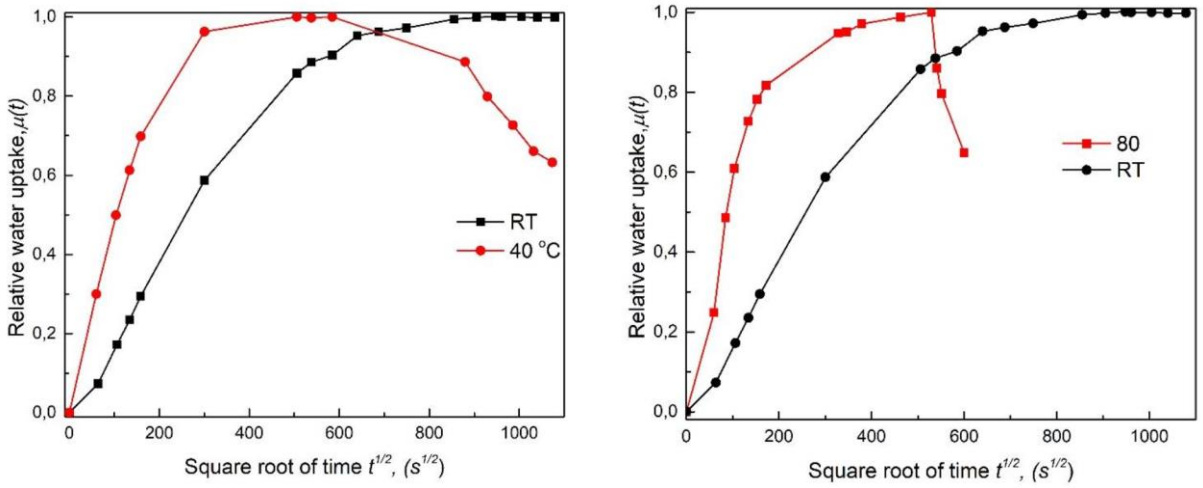

Figure 19 Relative water uptake μ(t), as a function of square root of immersion time at different temperatures in 3.5% NaCl for circular adhesive (20 mm dia & 720 ± 15 μm thickness)

It has to be taken into account that only Figure 18 is presented as the exemplary one with the data fitted to equations (3) and (4) and all other figures are presented simply as data points.

The same experiments were also done at elevated temperatures (40 °C and 80 °C) and it can be seen clearly that, from Figure 19 after a linear increase with time and saturation, the adhesive starts to lose weight. Subsequently, leaching behavior was observed where the salt solution also turned brown. This anomalous behavior is often associated with surface mass loss or resin peeling [19]. The increase in temperature also increased the kinetics of water uptake rapidly which is also reflected in the increase in diffusion coefficient.

The gravimetric experiments were also performed in deionized water to investigate the effect of ions on the water uptake kinetics.

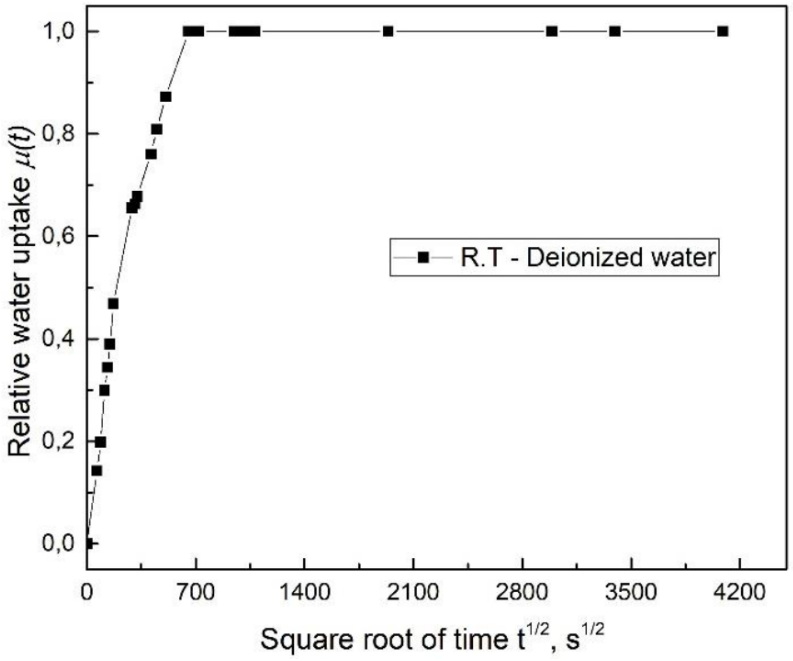

Figure 20 Relative water uptake μ(t), as a function of square root of immersion time at 25 ± 1 ^{o}C in deionized water for circular adhesive (18 mm dia & 420 ± 20 μm thickness)

Similar to salt solution, the water uptake curve for deionized water also followed Fickian behavior with linear increase in time initially followed by complete saturation. The saturation has remained constant for more than 9 months as well. The kinetics of water uptake is slightly faster when compared with the salt water however the maximal water absorption is not significantly different.

At higher temperature, no visible leaching was observed for deionized water tests. Instead there was a slight weight increase from the saturation point. However, prolonged experiments are necessary to deduce the trend. It has to be also noted that getting data points for experiments at 80 ^{o}C is challenging because of the very fast uptake kinetics.

In summary, water sorption curves follow typical Fickian behavior for both salt water and deionized water at room temperature. Increase in temperature increases the kinetics which is reflected in the diffusion coefficients (Table 2). In salt water, increase in temperature results in leaching of the adhesive inducing an anomaly from the Fickian behavior. The kinetics of water uptake is quite comparable between both salt and deionized water. There is a slight reduction in maximal water absorption in salt water which can be attributed to reduction in the chemical potential of water in the presence of salt.

EIS - Water uptake

As noted in the experimental section, the impedance spectra was performed at high frequencies (1 Hz – 100 KHz) where the adhesive behaved perfectly capacitive (Figure 21).

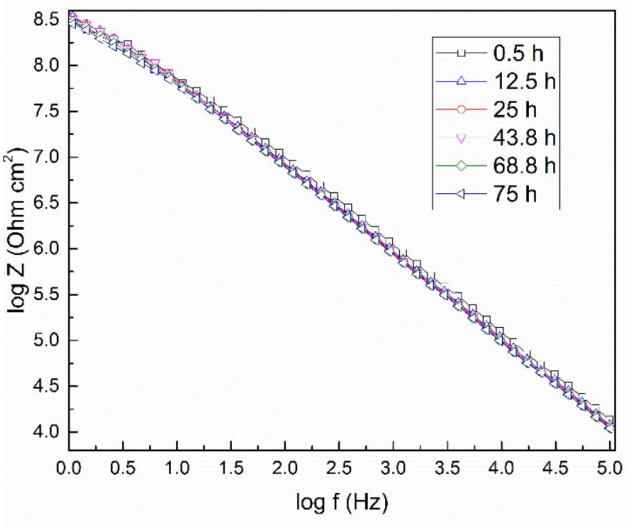

Figure 21 Impedance spectra of adhesive film at different durations of water uptake

It has been shown by A. Miszczyk et al. [20], that the values of water uptake obtained by plotting the capacitances obtained at higher frequencies over time are closer to the ones obtained by gravimetric analysis. Thus, the capacitances obtained at 10 KHz was plotted over time in Fig 22. It can be seen that, initially for the first few hours, the capacitances increase rapidly with time as water percolates into the micro-voids and free volume existing in the adhesive. Later, the first saturation effects can be observed where the capacitance is only slowly increasing over time. The further increase of capacitance with time can be attributed to either swelling of the adhesive or to the fact water can cluster underneath the adhesive.

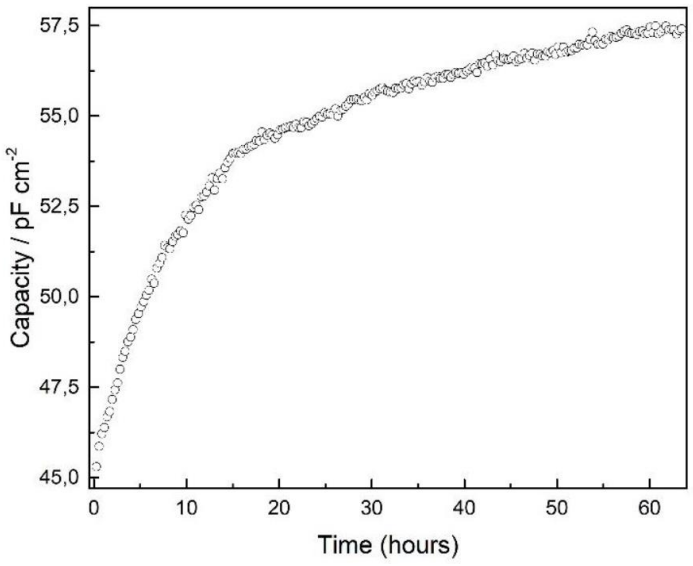

Figure 22 Capacitance time curve for the MMA adhesive (120 ± 20 µm) system at room temperature

The natural logarithm of capacitance plotted versus the square root of time is shown in Fig 23 and it can be seen that the water uptake obeys Fick's law in the linear zone of the data.

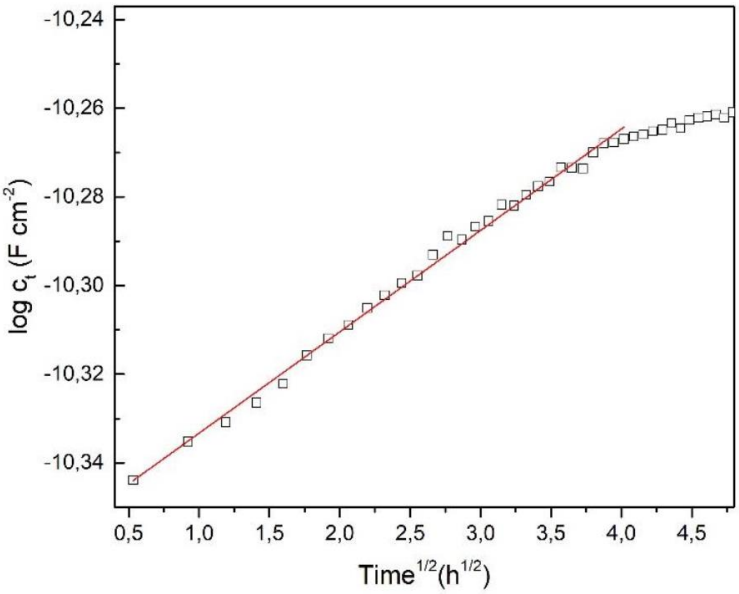

Figure 23 Capacitance-time curve in the linear region

By fitting the linear part of the data and by extracting the values of slope and intercept, the diffusion coefficient for the water uptake can be calculated using equation 6 [21].

$$\frac{log\ c_t - log\ c_0}{log\ c_s - log\ c_0} = \frac{2\sqrt{t}}{L\sqrt{\pi}}\sqrt{D} \tag{6}$$

where c_t , c_s and c_o are capacitances at time t, saturation and extrapolated to zero respectively.

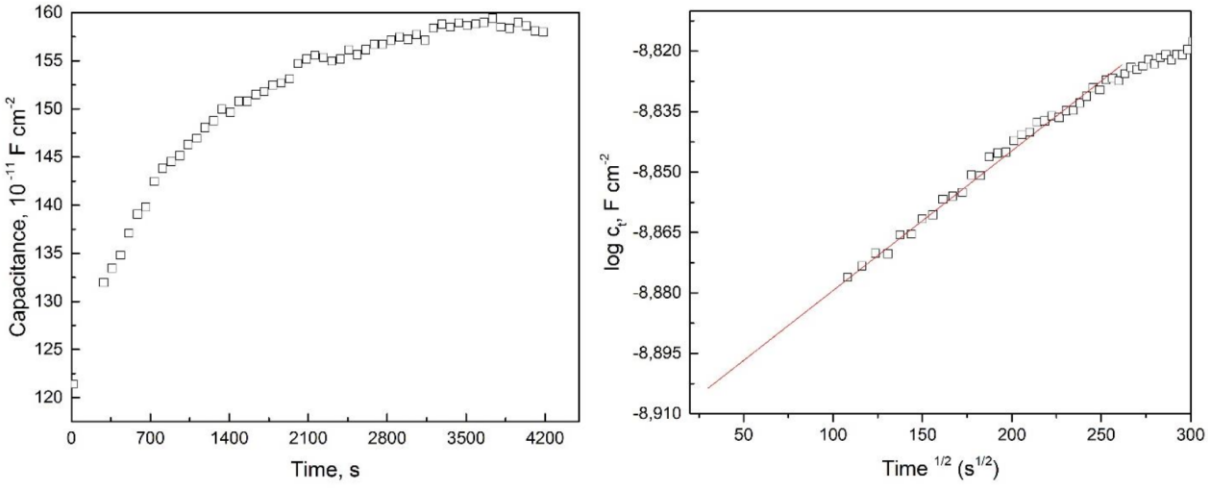

Figure 24 Capacitance-time graphs for adhesive (280 ± 20 µm) at 40 ºC with 3.5 % NaCl electrolyte

The diffusion coefficient obtained using EIS at room temperature was very similar to the one obtained by Bordes et al., for the adhesive Araldite 2015 using classical gravimetric technique [22]. Similarly, the EIS measurement was also carried out at 40 °C and the capacitance graphs are shown in Fig 24.

The diffusion coefficient obtained at 40 °C is an order faster than the one obtained at room temperature. Increase in temperature increases the chain mobility of the polymer as well facilitating faster water absorption which is reflected in the uptake kinetics. Thus, it can be concluded that the combined effort of water and increased temperature will result in faster saturation of the adhesive.

The maximal water absorption (φ) can be calculated using the Brasher-Kingsburry equation

$$\varphi(\%) = \frac{log(\frac{C_t}{C_o})}{log\, \varepsilon_w} \quad (7)$$

where c_t and c_o are capacitances at time t and extrapolated to zero respectively, ε_w is the dielectric constant of water (78.3).

It can be noted from table 2 that the maximal water absorption for both R.T and 40 °C is around 5.5 % and it is almost twice that of the ones obtained from gravimetric technique.

Table 2 Parameters and a summary of results related to diffusion of water into an MMA adhesive characterized by gravimetry and by EIS.

Technique	**Electrolyte**	**Temperature (°C)**	**D (10^{-13} m^2s^{-1})**	**W (%)**
EIS	3.5 % NaCl	R.T	0.89 ± 0.2	5.9
EIS	3.5 % NaCl	40	6.7	5.6
Gravimetric	DI	RT	4.1 ± 1	2.5
Gravimetric	DI	40	14.4 ± 0.2	2.9
Gravimetric	3.5 % NaCl	RT	3.3 ± 0.25	1.9
Gravimetric	3.5 % NaCl	40	17.8 ± 1.1	1.9
Gravimetric	3.5 % NaCl	80	79.6 ± 15.5	3.3

FTIR- Water uptake

For the water uptake measurements using ATR-FTIR, the spectra of adhesive was taken initially as the background reference upon which the measurements were performed. Fig 25 illustrates the peak evolution over time upon exposure to the electrolyte solution.

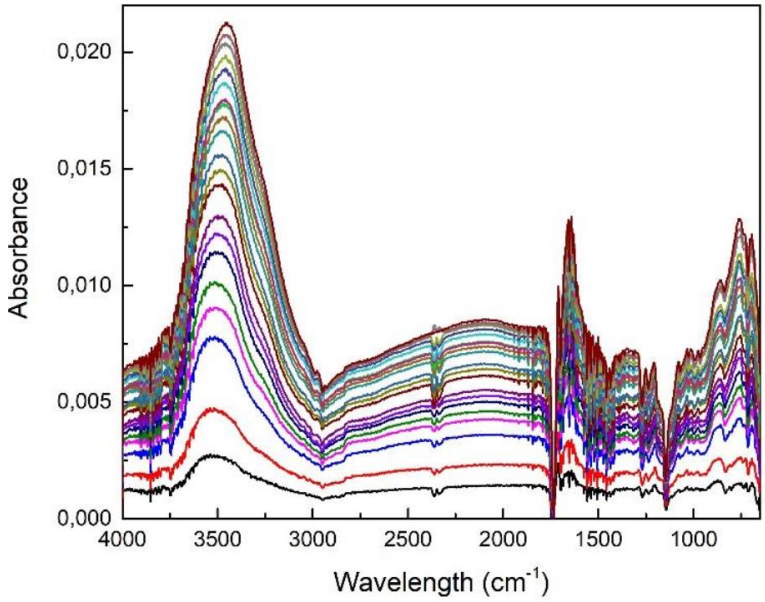

Figure 25 ATR-FTIR spectrum obtained after exposure to 3.5 % NaCl solution over 24 hours

Upon exposure, IR-spectra show a broad and strong band between 3700 and 3000 cm^{-1} that can be attributed to hydroxyl (OH-) stretching vibration. Thus, the water uptake kinetics can be monitored by observing the increase in area of hydroxyl absorbance peak over time. The diffusion coefficient can be calculated using simplified Fieldson-Barbari equation by measuring the absorbance over time

$$ln(1-\frac{A_t}{A_s}) = ln\left(\frac{4}{\pi}\right) - \frac{D\pi^2}{4L^2}t \quad (8)$$

where A_t and A_s are absorbance values at time t and saturation. *D* is the diffusion coefficient, *L* is the thickness of the adhesive.

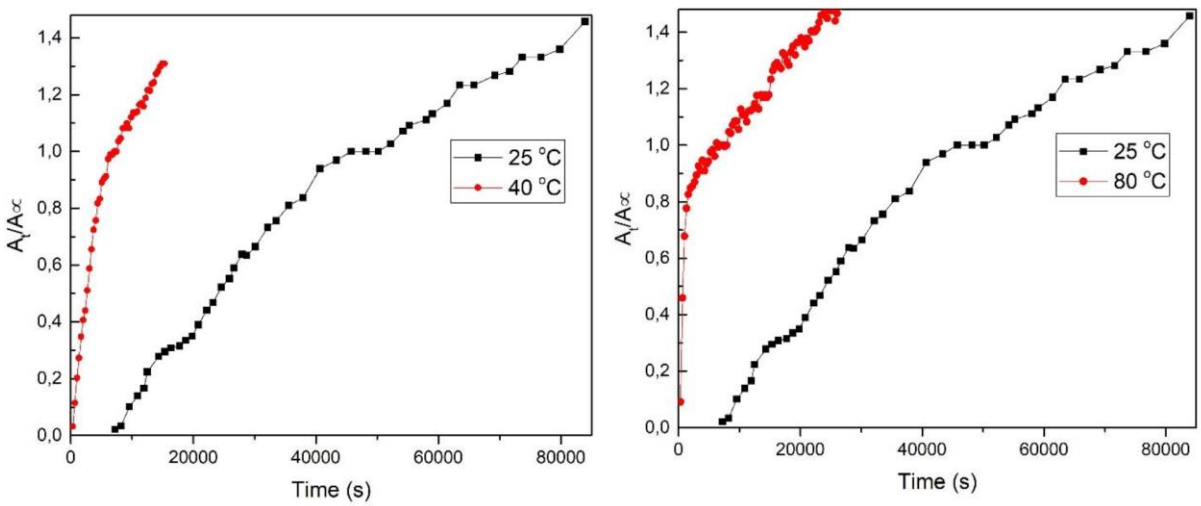

Figure 26 Absorbance increase of OH^- peak as a function of exposure time for deionized water at different temperatures

Plotting the absorbance as a function of time (as well as square root of time, plot not shown here) showed linear correlation initially keeping up with the Fickian kinetics (Figure 26). Clearly, the uptake kinetics also increased with time. However, at the later stages there was obvious deviation from the Fickian behavior. To see whether this deviation could be explained by swelling of the polymer, the original Fieldson-Barbari equation was modified with a swelling coefficient term $\frac{SC}{L}\sqrt{t}$, similar to the one performed by Nguyen et al., for EIS [23].

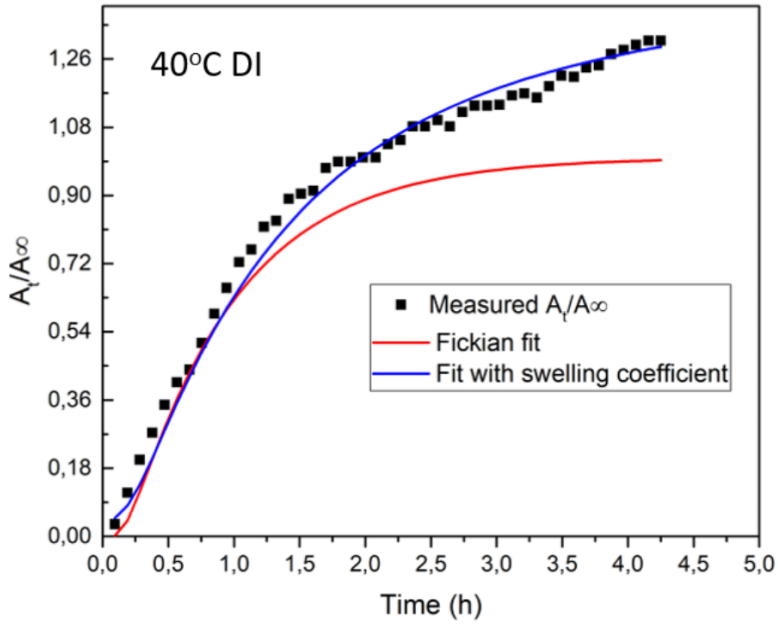

Figure 27 Absorbance increase of OH^- peak as a function of exposure time for deionized water at 40 °C fitted with swelling coefficient

One of the exemplary results of fitting the water uptake results with swelling coefficient can be seen in Fig 27. Thus, it is possible to explain the deviation from Fickian behavior with incorporation of a swelling coefficient. However, it is very important to do long term IR measurements to see if there is consistent structural realignment in the polymer over time. It will also be beneficial to physically measure the swelling of the adhesive as well. The parameters obtained from ATR-FTIR study is summarized in Table 3.

Although the values for *D* obtained using the conventional gravimetric technique and ATR-FTIR are consistent with each other, there is indeed a noticeable difference between gravimetry and EIS, with lower *D* values obtained from latter. It has to be also noted that an overestimation of maximal water absorption is observed in EIS when compared with the gravimetric data, which is consistent with other studies in the literature. Estimation of water absorption kinetics from EIS is dependent on many things such as – assumption of saturation capacitance, the method of capacitance calculation (high frequency method vs fitting the curve) etc. It has to be also noted that in EIS, one dimensional diffusion is measured in contrast to gravimetric technique where a free standing film is used. The direction of porosity in the polymer (perpendicular or parallel to the direction of diffusion) also influences the value of diffusion coefficient. In particular, the exaggerated values of maximal water absorption obtained by EIS have been attributed to increased swelling of the polymer as it is attached to the steel substrate.

Table 3 Parameters and a summary of results related to diffusion of water into an MMA adhesive characterized by ATR-FTIR

Technique	Electrolyte	Temperature (^{o}C)	D (10^{-13} m^2s^{-1})
FTIR	DI	25	5.5
FTIR	DI	40	48.7
FTIR	DI	80	150
FTIR	3.5 % NaCl	25	3.3
FTIR	3.5 % NaCl	40	18.1

3.2. Interface characterization

3.2.1. Mode I fracture toughness

The general trend for the DCB specimens is similar for all the tested specimens non-aged vs. aged (see Fig. 28). The crack initiation is reflected in the load displacement curve with a

drop in the load or a change in the slope (point 1). However, after this first drop, which is consistent for all specimens, there is an increase again in the load as function of the displacement (point 1 to point 2). This can be attributed to the build-up of almost a symmetric fracture process zone (FPZ) ahead of the crack tip (see Fig. 29). To be more precise, there is a competition between the energies dissipated via the adhesive plastic deformation via the FPZ and the crack growth “creating a new fracture surface”. This phenomena was recently reported and analyzed by Tao et al [24]. Once this build-up of FPZ is achieved, the crack starts propagating again. Based on the variation amongst the specimens in the build-up process of the FPZ ahead of the crack tip, the segment of this load increase varies. Moreover, the propagation during this time is not always stable. Sometimes the crack growth is gradual, leading to a gradual softening in the load-displacement curve (point 2 to point 3). Some other times, the growth is not stable and “sudden” leading to a sharp/sudden drop in the load (point 3 to 4). This can be easily confirmed with the DIC images captured in-situ during testing as shown in Fig. 30.

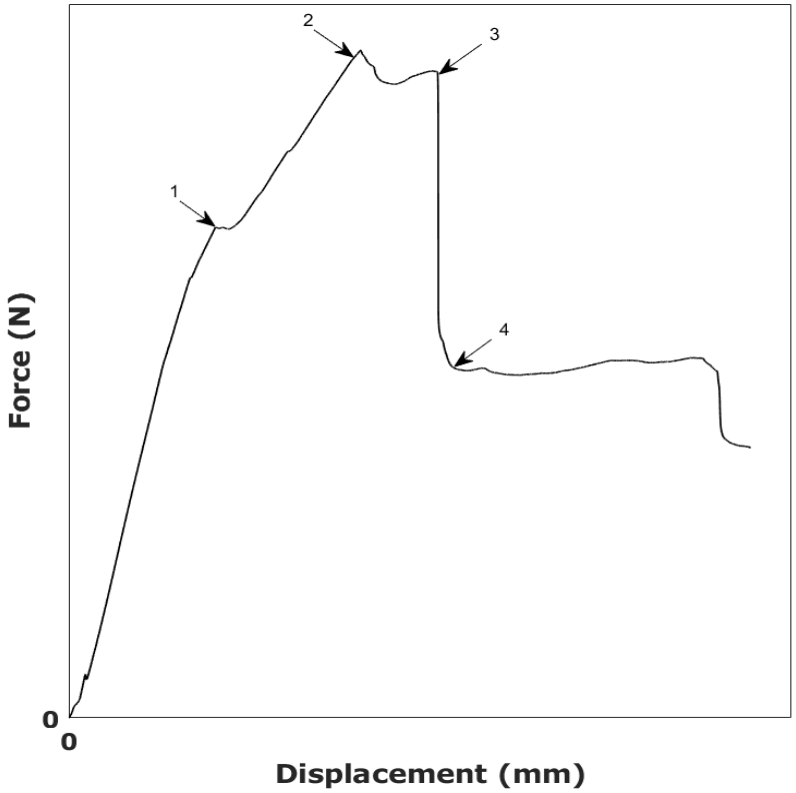

Figure 28 A schematic of the load-displacement response for the DCB specimens

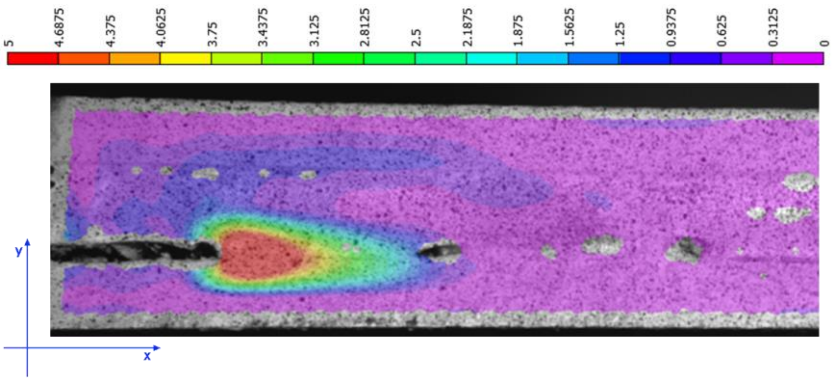

Figure 29 ε_{yy} strain contour map (in %) captured using DIC ahead of the crack tip

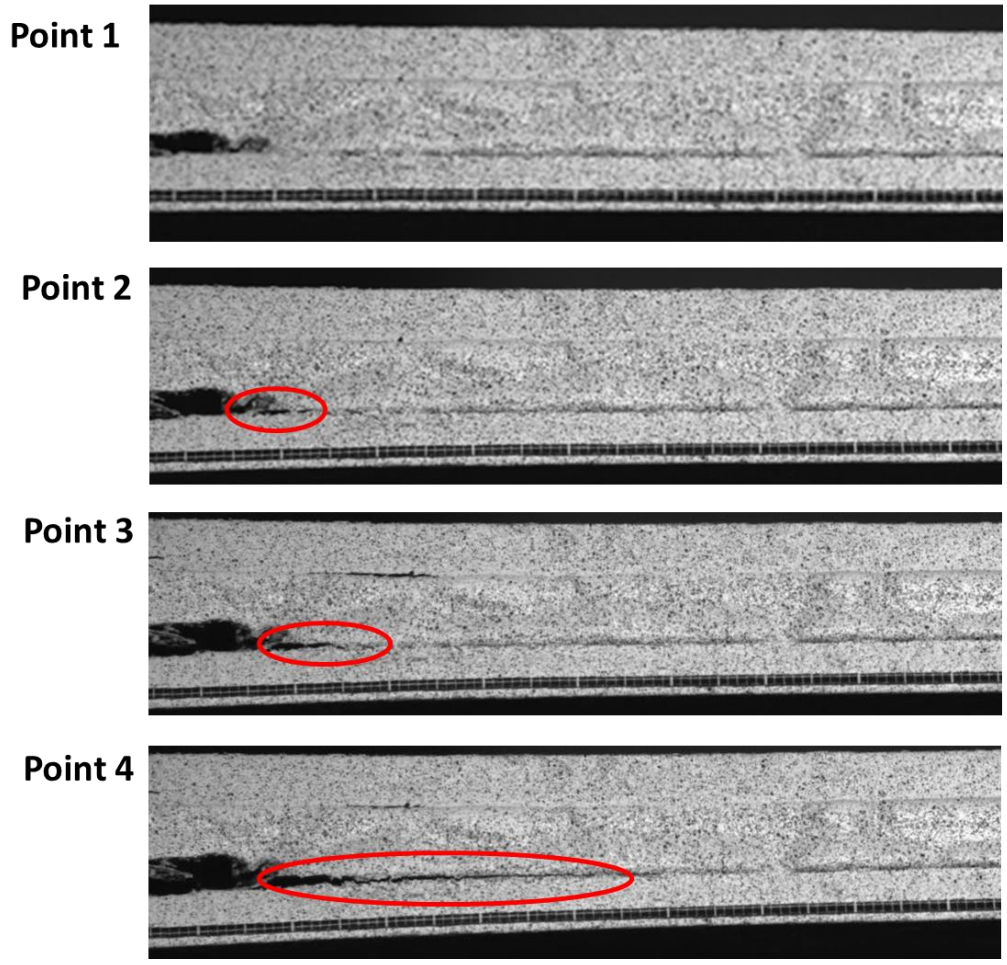

Figure 30 Crack propagation captured by the DIC camera corresponding to the load points 1, 2, 3 and 4

In both non-aged and 6 weeks-aged specimens, two specimens, out of five repeats, experienced a combined effect of the crack growth (see Fig. 31) where the Teflon film was inserted and another crack initiating at the other interface. The reason for such phenomena can be easily explained in the light of the strain contour maps captured by the DIC (see Fig. 31). Due to the loading condition, normal strain is imposed at the other interface leading to the competition between the two steel/adhesive interfaces. These 2 specimens for each

condition are highlighted with the dashed line in Figure 32. In addition, The FPZ build-up region/segment differs when it comes to comparing the non-aged vs. the 6 weeks-aged specimens. In the case of the 6 weeks-aged specimens, the FPZ build-up segment is larger (see Fig. 33). This might be the effect of the ageing of the adhesive resulting into a softer/more ductile nature.

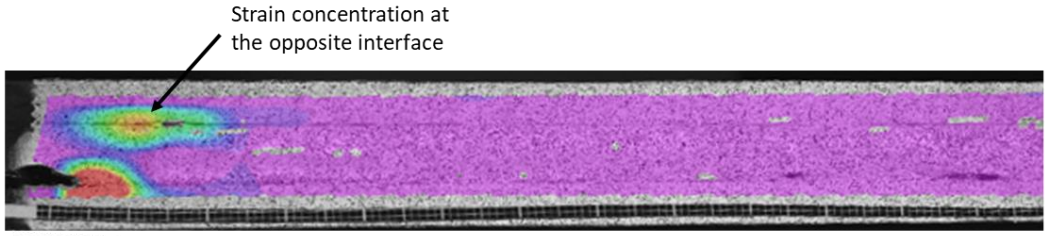

Figure 31 Strain concentration at the crack tip interface and the opposite interface due to bending of the DCB arms during testing

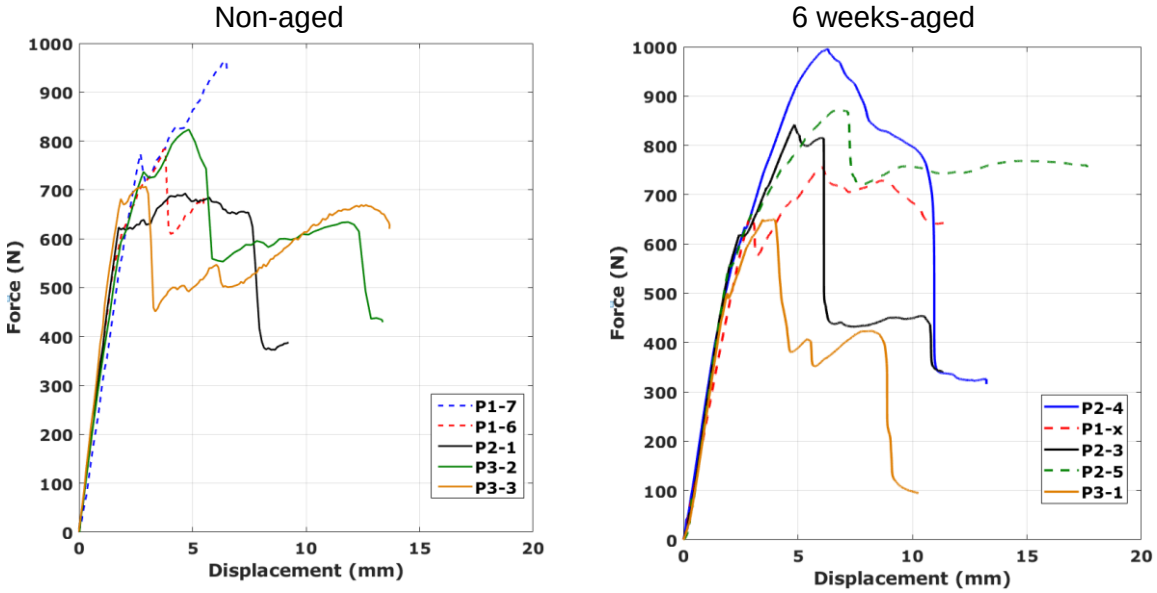

Figure 32 Load-displacement curves of the non-aged vs. 6 weeks-aged DCB specimens

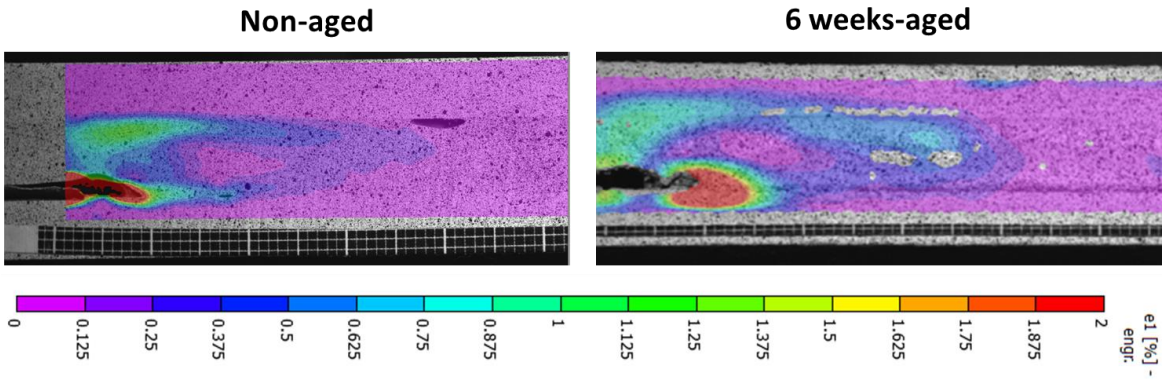

Figure 33 Principal strain contour map ahead of the crack tip for both non-aged and 6 weeks-aged cases right before crack propagation

It is clear from the fractured surface analysis (see Fig. 34) that there exist different fracture regions which complement the understanding of the global response. For the non-aged specimens, no significant difference in the color is observed ahead of the initial crack tip, while for the aged specimens, the first region is characterized by a different color and a very short length (see Fig. 35). This indicates the moisture ingress region due to ageing, which governs the initial drop in the load-displacement curve. This is followed by a much longer non-affected/aged region. The non-affected interface by the moisture could explain the similarity in the phenomenon of the FPZ build-up following the first load drop between the aged and the non-aged specimens as indicated by the DIC principal strain contour maps (see Fig. 33). In addition, along the two edges a trace of the steel corrosion due to the water/moisture ingress is clear, represented by the change in color similar to the color at the crack tip.

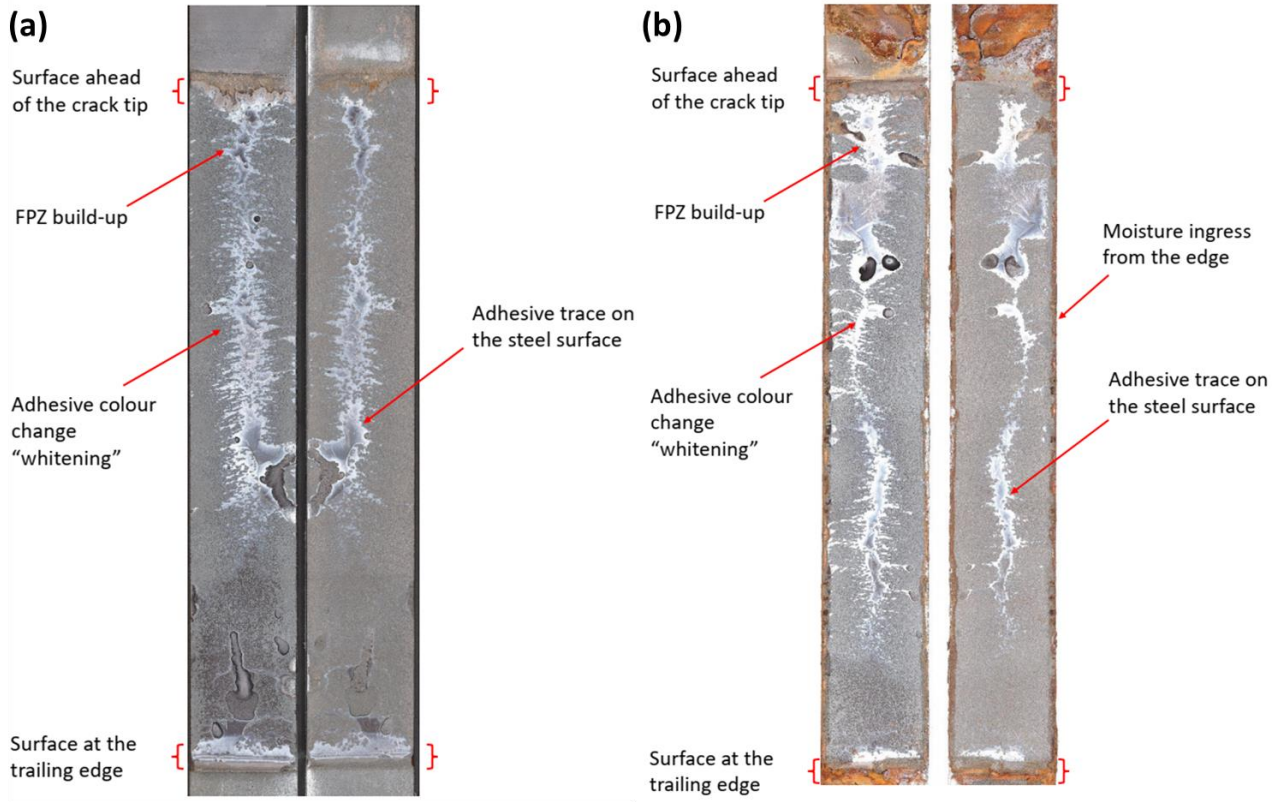

Figure 34 Optical microscopy scans of (a) non-aged vs. (b) 6 weeks-aged DCB specimen

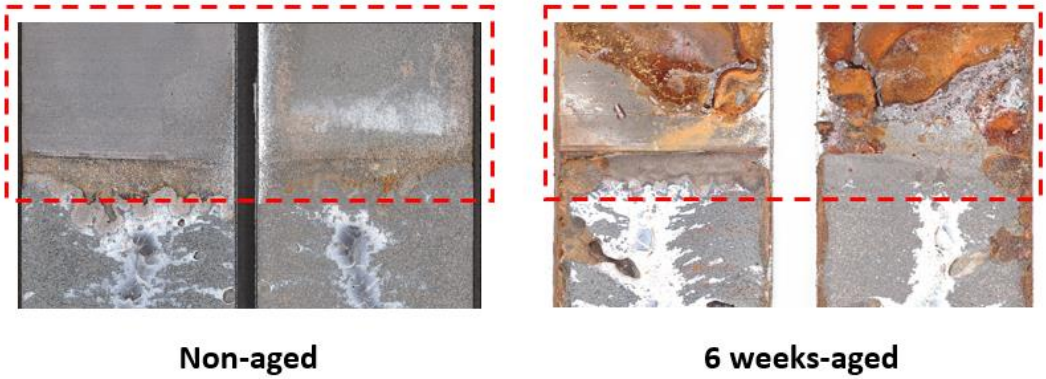

Figure 35 Zoomed-in microscopy of the surface ahead of the crack tip

Along the specimens length, there is a clear difference between the center and the edges of the fractured surfaces. In both non-aged and aged cases, there exists a trace of the adhesive (cohesive failure) along the center while the edges are mainly the steel surface (adhesive failure). In order to understand this phenomenon, it is important to investigate the stress state across the width of the specimen. The shape of the plastic zone ahead of the crack tip (see Fig. 36a) depends mainly on the stress state being plane-stress or plane-strain [25]. The shape of the plane-strain plastic zone changes from a plane-stress state near the surfaces to a plane-strain state in the interior. This leads to a dog-bone like shape of the plastic zone ahead of the crack tip (see Fig. 36b). Although the plastic zone at the center is smaller than near the edges, the high tri-axial stress that exists at the center (referred to as plastic constraint) causes crack growth to occur there first, under both static and fatigue conditions. The net effect of this is that cracks advance in a curved shape, in a wide specimen, with the crack front leading in the center regions of the plate but lagging behind at the edges.

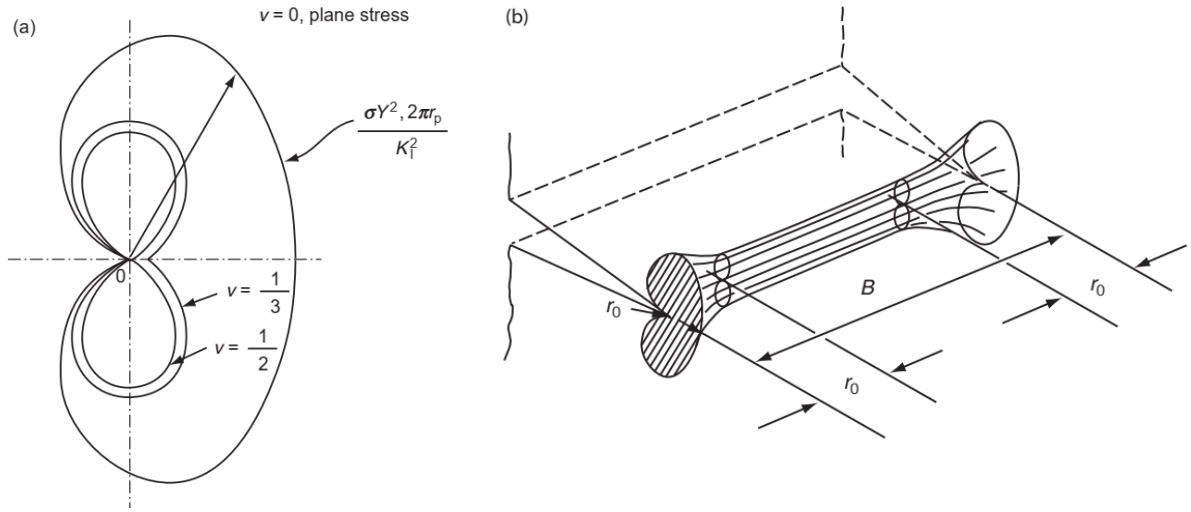

Figure 36 A schematic of (a) 2D Plastic zone projection in plane strain and plane-stress states, (b) 3D dog-bone like plastic zone across the width [25]

According to the ASTM D5528 [5], there exist three data reduction techniques for the calculation of the interlaminar fracture toughness in mode I (G_{Ic}). These methods are: i) the modified beam theory (MBT), ii) the compliance calibration method (CC) and iii) the modified compliance calibration method (MCC). The good news is that the G_{Ic} determined values from the three techniques differ only by a minor margin (~ 3.1%). However, the MBT approach results in the most conservative values of G_{Ic} [5]. Thus, this technique is the one used in this report for the data analysis. The MBT theory calculates the strain energy release rate G_{Ic} assuming there is no rotation at the delamination/crack front, as follows:

$$G_I = \frac{3P\delta}{2ba} \tag{9}$$

where:

P = applied load,

δ = the measured displacement,

b = the specimen width, and

a = the delamination length

In practice, this assumption will overestimate the values of G_{Ic} because the DCB is not perfectly clamped (built-in). In order to account for this rotation, the DCB specimen is assumed to have a longer crack/delamination length $a + |\Delta|$, where $|\Delta|$ can be determined from a graph of the cubic root of the compliance, $C^{1/3}$, as a function of the delamination length. The intersection of the least squares fit with the x-axis is $|\Delta|$, and the compliance, C, is the displacement-to-load ratio, δ/P, and the corresponding points are determined as function of the visually observed delamination length starting from the onset point. The calculated value for $|\Delta|$ in this study is ~ 18.6.The Mode I interlaminar fracture toughness is thus determined as:

$$G_I = \frac{3P\delta}{2b(a + |\Delta|)} \tag{10}$$

R-curves are frequently used in order to predict the response of the material during damage propagation, and are obtained by plotting G_I against the crack extension. Due to the scatter in the data after the crack onset as previously highlighted, the calculations in this report are limited only to the initiation fracture toughness without considering the R-curve. The non-aged vs. the 6 weeks-aged energy release rates, calculated based on the visual observation,

are depicted in Fig. 37. Taking the standard deviation, the scatter, of the data into account, this suggests that the 6-weeks ageing investigated in this study did not affect the initiation fracture toughness significantly.

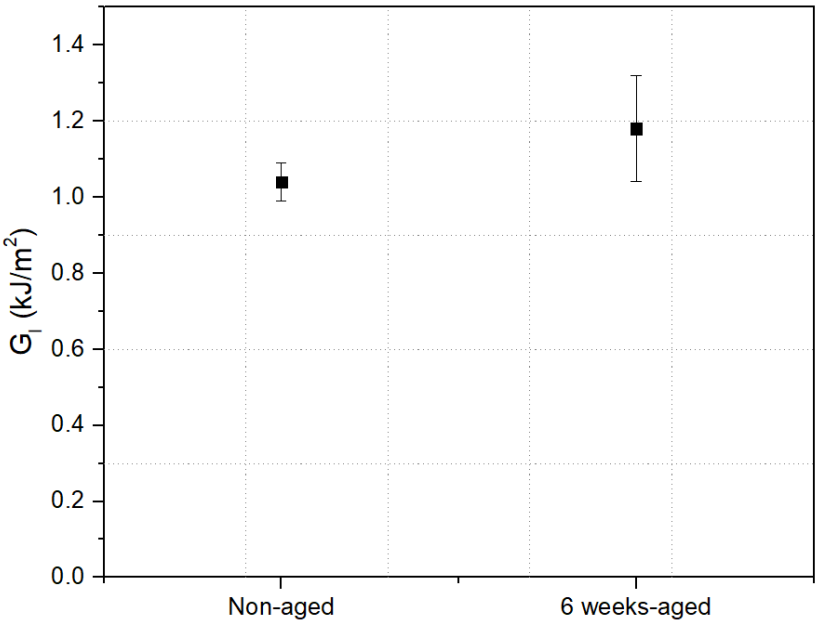

Figure 37 Energy release rate as function of the ageing duration

3.2.2. Mode II fracture toughness

In order to evaluate the effect of the adhesive layer thickness on the shear strength of the joints, average shear stress versus shear strain across the adhesive layer curves were plotted in Fig. 38a. The cases examined were for values of h = 3, 5, 8, 10, and 13 mm and no pre-crack (a_0 = 0). The red marks indicate the onset of cracking. The results show that the joint strength decreased by increasing the adhesive layer thickness. Also, the maximum shear strain across the adhesive layer decreased as the adhesive thickness increased. Fig. 38b shows the degree of crack extension as a function of the shear strain across the adhesive layer for the cases mentioned above. In all these specimens, the crack grew 5-15 mm gradually as the shear stress and shear strain across the adhesive layer increased. The shear strain across the adhesive layer at the onset of cracking decreased as the adhesive layer thickness increased.

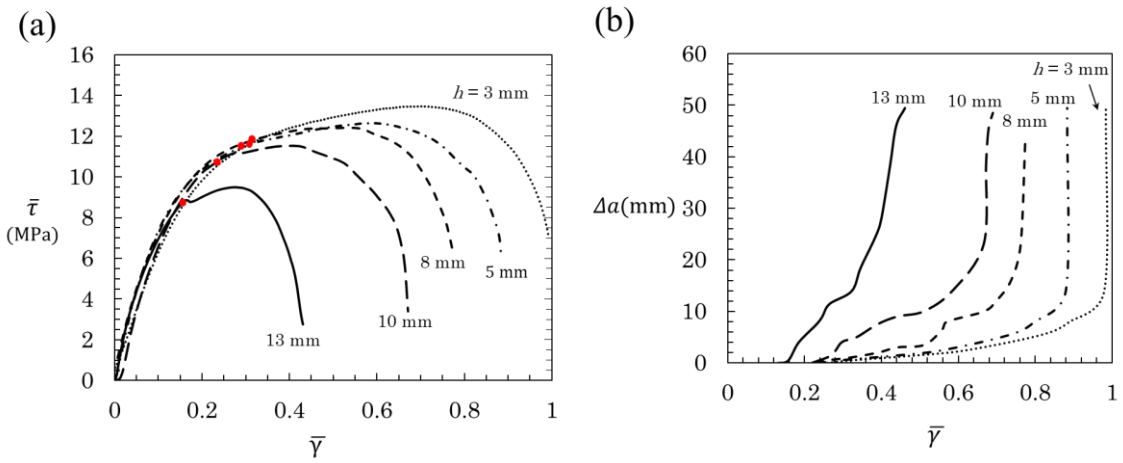

Figure 38: Effect of the adhesive thickness on samples with a_0 = 0 (no pre-crack). (a) Average shear stress-shear strain across the adhesive layer curves (red marks on the curves shows a = 1 mm), (b) crack growth versus shear strain across the adhesive layer.

In order to evaluate the effect of pre-crack length, specimens with adhesive layer thickness of h = 3 mm and pre-crack length of 0, 10, and 20 mm are compared as representative cases in Fig. 39. The average shear stress versus shear strain across the adhesive layer is compared in Fig. 39a. Red marks are used to show the crack length (a= 1, 5, and 10 mm) at different stages of deformation. The stiffness, the shear strength and the shear strain of the joints, decreased as the pre-crack length increased. Fig. 39b shows the effect of pre-crack length on the crack extension of specimens with adhesive layer thickness of h = 3 mm as a function of the shear strain across the adhesive layer. For values of shear strain less than 0.7, the crack extension followed the same profile while for higher values of strain the profiles were changing. For the cases of a_0 = 20 mm and a_0 = 10 mm, quick crack extension occurred for shear strain values of 0.79 and 0.92, respectively.

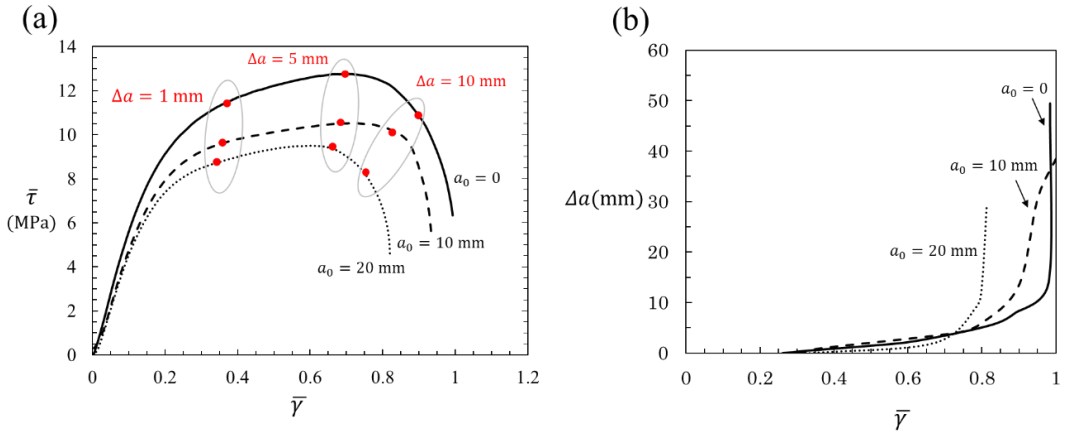

Figure 39: Effect of the pre-crack length on specimens with adhesive layer thickness of 3 mm. (a) average shear stress as a function of the shear strain across the adhesive layer

(marks on the curves shows a = 1, 5, and 10 mm), (b) crack growth versus the shear strain across the adhesive layer for these cases.

Fig. 40 shows the effect of the adhesive thickness on the mechanical response of the specimens with a_0 = 10 mm (a, b, c) and a_0 = 20 mm (d, e, f). Fig. 40(a, d) shows the average shear stress versus shear strain across the adhesive layers obtained for specimens with a_0 = 10 mm and a_0 = 20 mm, respectively. Fig. 40(b, e) shows the degree of crack extension versus shear strain across the adhesive layer obtained for these cases and Fig. 40(c, f) shows the shear strain across the adhesive layer at the onset of cracking and at peak load as a function of the adhesive layer thickness. The results show that pre-crack length has no significant effect in the shear strain across the adhesive layer corresponding to the crack initiation. Also, it is observed that as the adhesive layer thickness increases to 10 and 13 mm, the crack happens at the peak load. These results can be used in the design of adhesive joints. In order to determine the mode I and mode II stress intensity factors at the crack front of TAST specimens, a numerical analysis was performed. Cracks with different lengths were incorporated into finite element models that were used to compute the stress intensity factors. The details of the modelling procedure will be presented in the next reports. For the sake of this report, they are briefly discussed as follows. Two numerical methodologies were employed. In the first method, the TAST geometry was modelled in ABAQUS and the stress intensity factors (dominated by Mode II) for the failure loads were obtained using FE. This is more useful for the cases where the adhesive is still in the elastic deformation regime. The second methodology was based on a cohesive zone modelling approach. The parameters of the traction-separation laws were determined using an inverse method, performing numerical iterations until good agreement was achieved between the experimental and numerical data. The area under the traction-separation law corresponds to the critical fracture energy. By making use of the numerical studies, experiments on TAST specimens with long crack (a_0= 20 mm), and theoretical analysis regarding interfacial fracture toughness, the Mode II MMA/steel interfacial fracture toughness (G_{IIC}) is found to be $4.2 \pm 0.5\ kJ/m^2$.

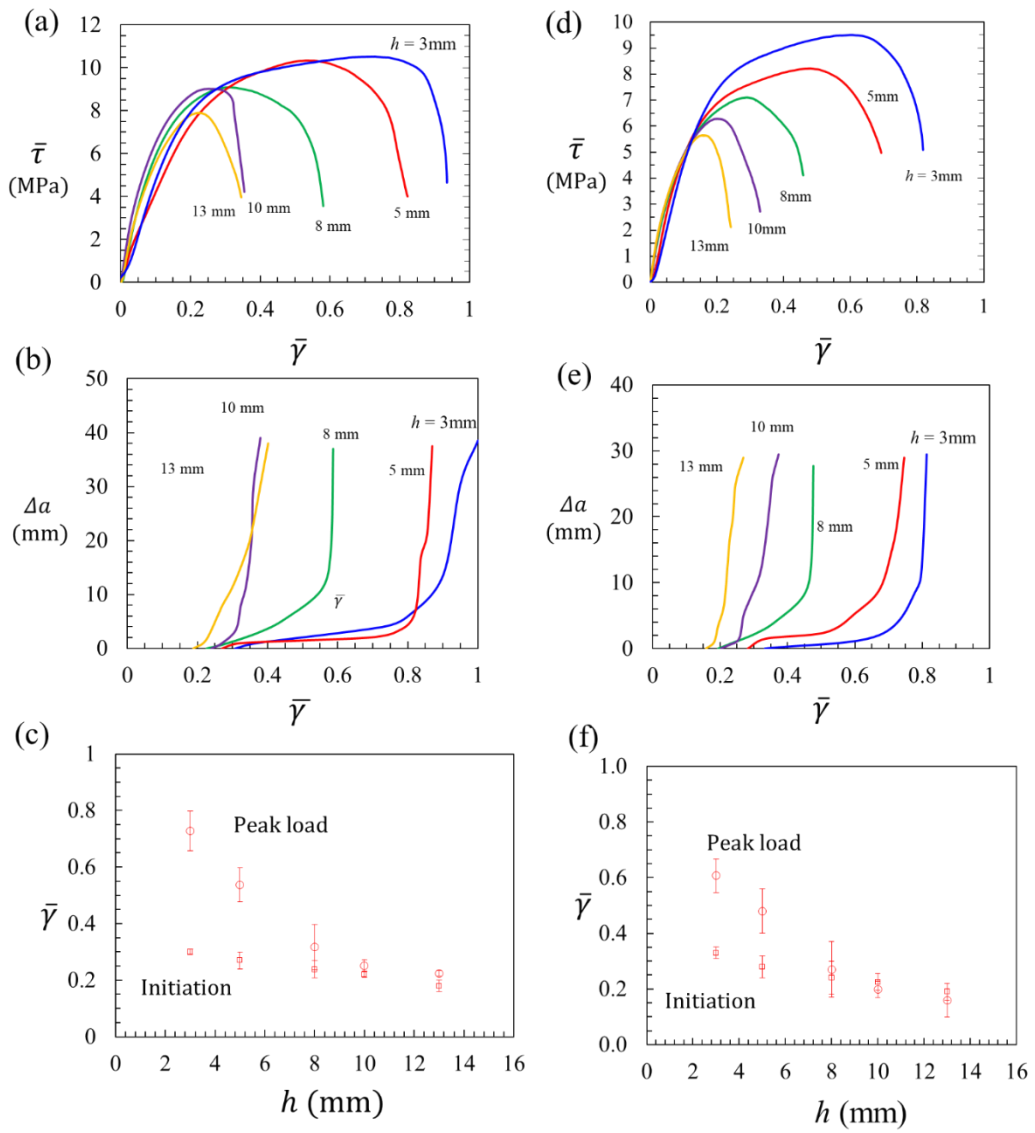

Figure 40: Experimental results for a_0 = 10 mm (a, b, c), and a_0 = 20 mm (d, e, f). a, d) plot the average shear stress versus the shear strain across the adhesive layer obtained from experiments, b, e) show the crack extension as a function of the shear strain across the adhesive layer, c, f) show the shear strains across the adhesive layer at crack initiation and peak load as a function of the adhesive layer thickness.

Aged Specimens

In order to evaluate the effect of salt-water diffusion and the subsequent corrosion of steel in the steel/adhesive interface, TAST specimens were environmentally aged and tested. TAST specimens with adhesive layer thickness of 5, 8, and 13 mm were fabricated. The specimens were exposed to an accelerated ageing cycle (80 °C, full immersion in salt-water, 3.5 % salinity). It is worth noting that the width of specimens is only 6.3 mm and therefore the exposure period needed to be shortened. Based on numerical simulations, salt-water

diffuses completely through the joint after 5 days. Hence, the mechanical testing of the joints was performed after 5 days of exposure.

Figure 41 shows the comparison between the average shear stress versus the shear strain for aged and un-aged specimens. The fracture of aged specimens is different from the un-aged ones. For these specimens, sudden failure takes place without progressive gradual crack growth. The fracture occurs at the steel/ adhesive interface (adhesive failure). The shear strength in the aged specimens is about 50% compared to the un-aged ones and their final shear strain is three times less. Using the similar analysis performed for non-aged specimens, the Mode II interfacial fracture toughness in aged specimens is measured to be $1.8 \pm 0.3\ kJ/m^2$. This value might change according to the aging time and conditions.

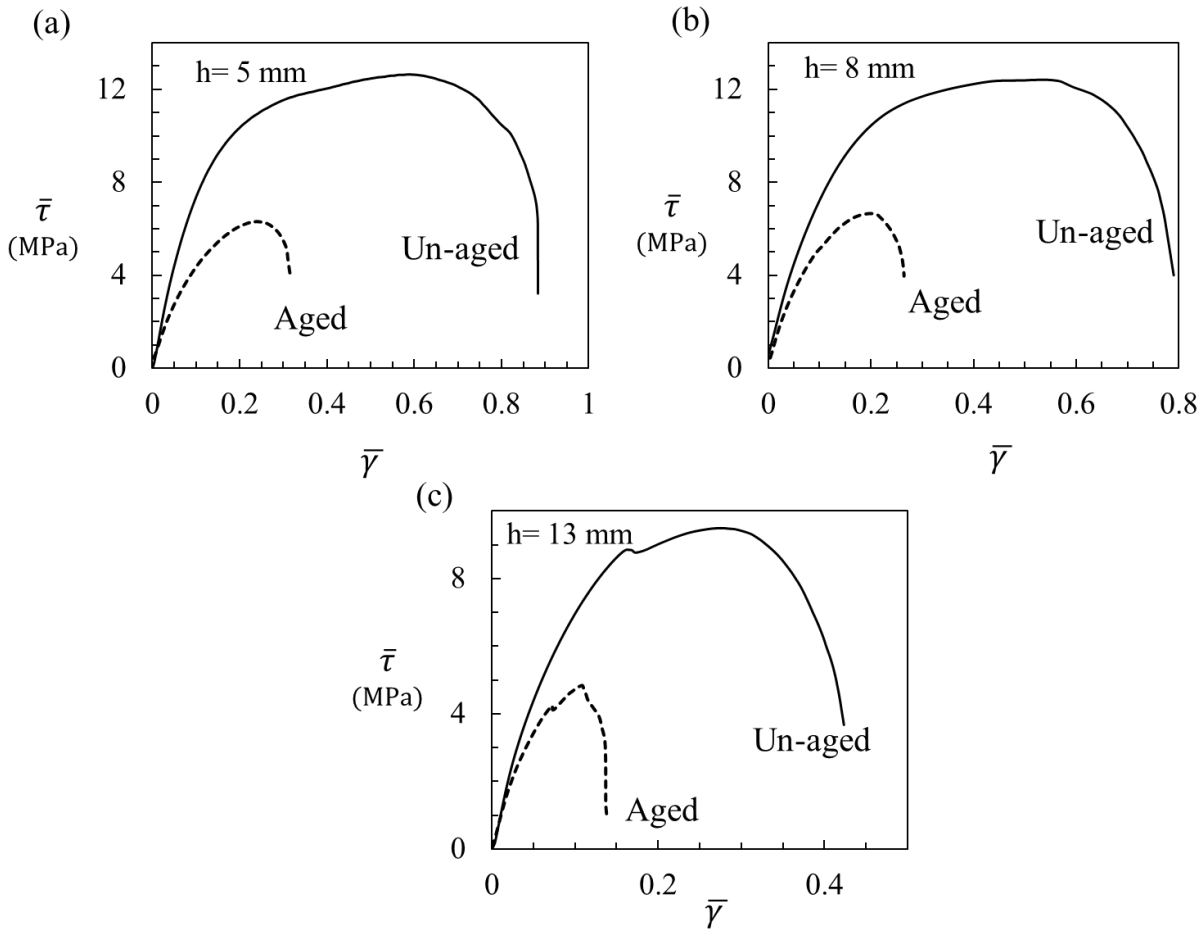

Figure 41: Average shear stress versus shear strain across the adhesive layer for specimens with adhesive layer thickness of (a) 5mm, (b) 8 mm, and (c) 13 mm.

Figure 42 shows the interfaces of the TAST specimen after failure for the unaged and the aged joints. Clear differences can be observed for the two cases. For the unaged joints, the damage took place at the interface, but the failure was cohesive and not adhesive as it was witnessed for the aged joints. In addition, the unaged joints displayed stress whitening across the width of the joint, showing that the adhesive layer resisted the loading entirely. For the

case of the aged specimens, a ring of moisture formed from the sides of the joints. This ring that was affected by moisture, did not deform plastically (as shown by the lack of stress whitening) and therefore reduced the resisting area of the joint. In addition, the failure mechanism was also different. For the unaged specimens, the damage initiated on both sides of the adhesive layer and then gradually propagated to the center until the two cracks connected and led the joint to fail cohesively. For the aged joint however, the damage only propagated at one side of the adhesive layer and led to delamination and adhesive failure.

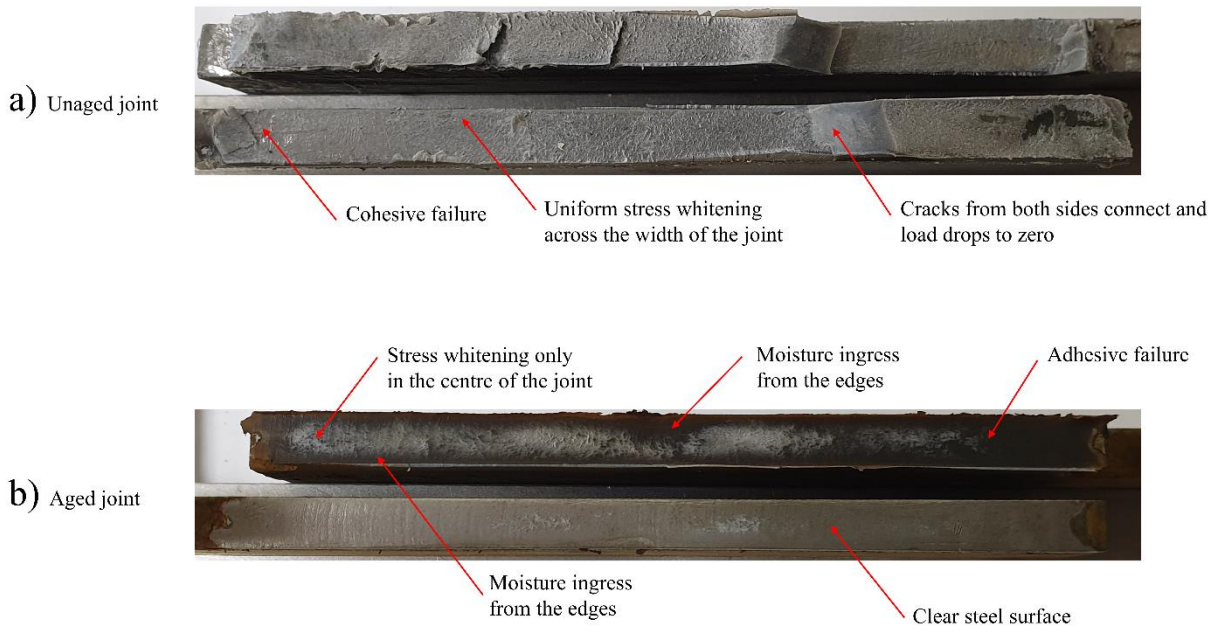

Figure 42: Failed interfaces of the TAST specimen for a) unaged and b) aged specimens

3.2.3. Delamination crack-growth

SKP – Interfacial Delamination

Figure 43 presents the SKP measurement of the steel sample covered with the adhesive. The origin of the x axis is close to the defect region containing the electrolyte 3.5 % NaCl solution. Two distinct potential levels characterize the SKP profile. Figure 43a shows the work function of the non-delaminated intact adhesive. After 2 hours of electrolyte addition it can be seen that the potential at the interface shifts cathodically resembling that of the bare metal.

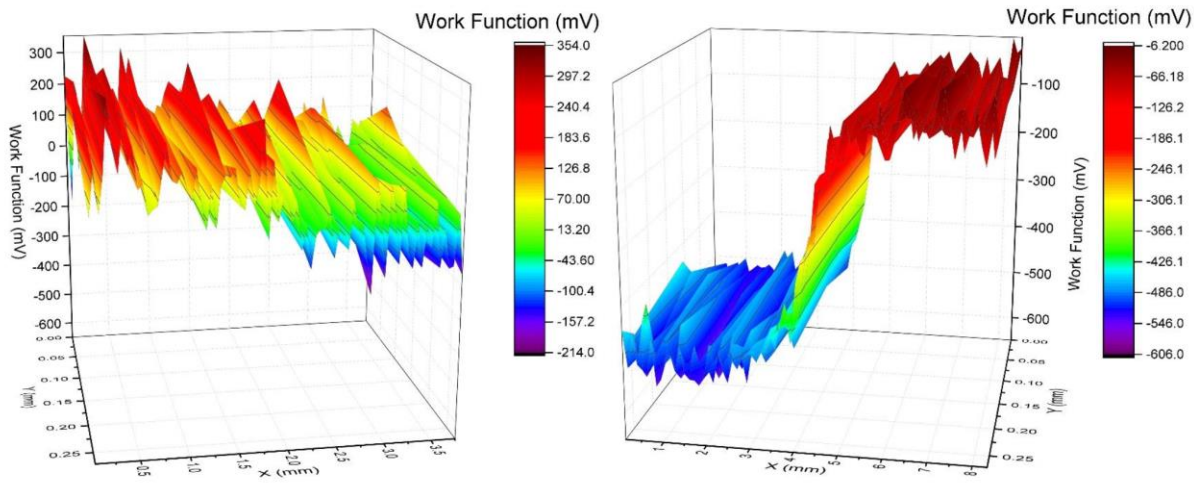

Figure 43 Work function before addition of electrolyte B) Work function profile after 2 hours of addition of electrolyte

The appearance of distinct potential levels is characteristic of cathodic delamination. At the localized defect, anodic metal dissolution occurs and oxygen diffuses through the adhesive to get reduced at the buried interface to hydroxyl ions.

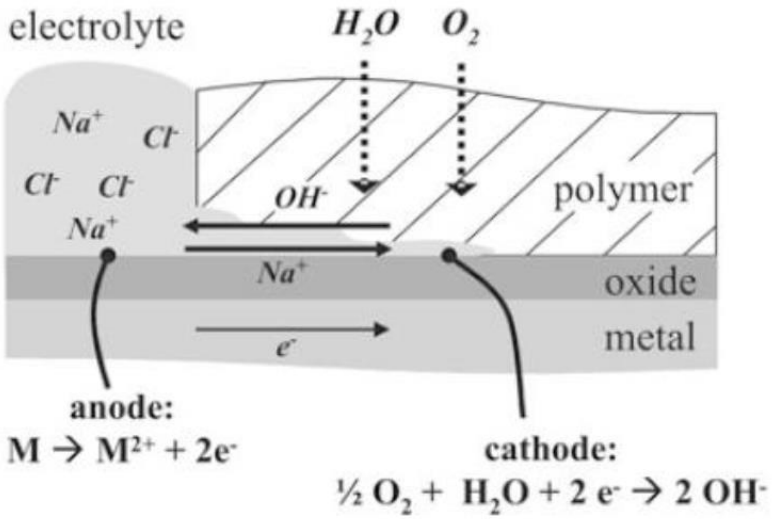

Figure 44 Schematic illustration of the cathodic delamination mechanism (9)

For compensation of charge, cations and electrons travel from the defect to the buried interface. Thus, after ingress, a potential similar to that one of the defect will be detected under the buried interface. This gives the possibility to track the cathodic delamination process as the transition from delaminated area to intact area is indicated by a rise in potential. The lateral deflection of the inflection point in S curve is commonly used as an indicator of the moving delamination front.

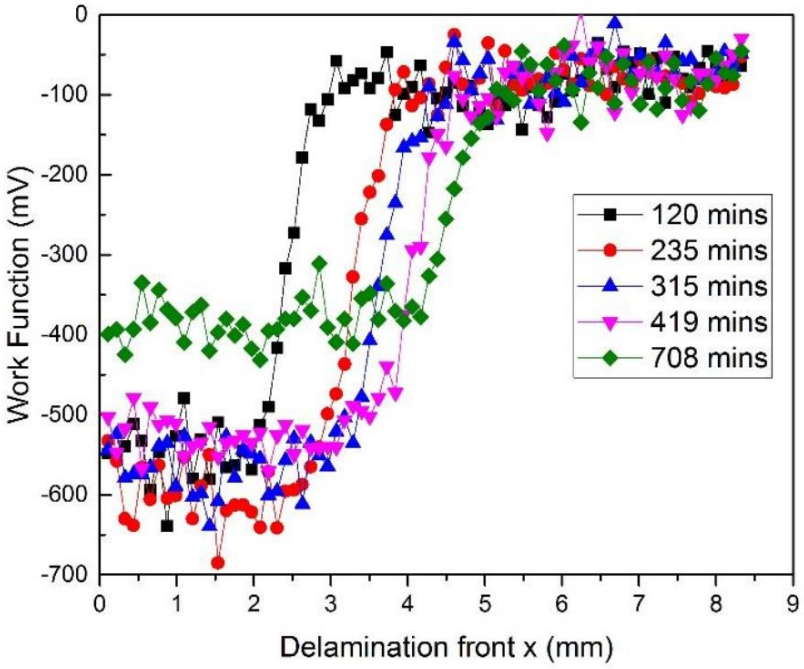

Figure 45 WF profiles as a function distance from the defect edge for different times as indicated. Electrolyte concentration in the defect is 3.5 % NaCl and test environment humidity 93%

As it can be seen in Fig 45, near the defect the work function is similar to that of bare steel and is followed by a sharp transition to the intact adhesive where the work function is higher. With increase in time, the delamination front keeps moving forward away from the defect zone indicating the distance until which the adhesive has delaminated from the metal. After 700 minutes, the potential at the defect is slightly more positive which is possibly due to the formation of corrosion products (iron oxides) at the defect zone.

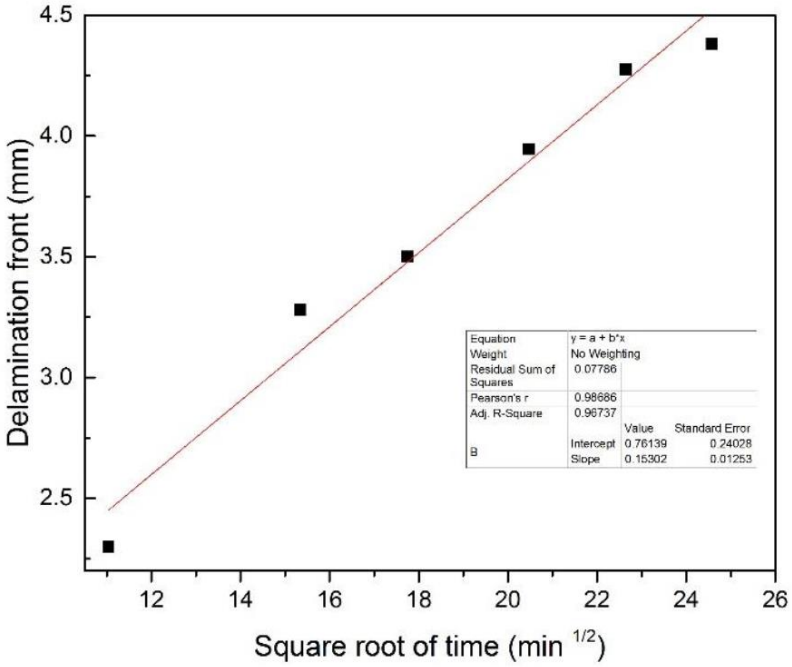

Figure 46 Delamination front position vs square root of time

Figure 46 shows the delamination front position as a function of the square root of time. The linear relationship indicates that the cationic transport along the interface is in fact the rate determining step. The average delamination rate was calculated to be 153 ± 6 μm/min$^{1/2}$. Though SKP is a very potent tool to investigate the delamination mechanism and subsequently the delamination kinetics, it should be clearly noted that the experiments were performed under an “open configuration” which requires the presence of an artificial defect. In reality, the bonded joint can act as a greater barrier to oxygen transport and hence, the kinetics can be substantially lower.

4. CONCLUSIONS

Based on the extensive experimental studies reported in this report, the following remarks can be made:

- Tensile dog-bone bulk adhesive

A full ageing campaign was carried out using salt-spray technique for tensile dog-bone bulk adhesive specimens. The objective of the campaign was to determine/evaluate the effect of the maritime environment on the degradation of the bulk adhesive properties. Comparison of the elastic modulus, strain and stress to failure, using weekly intervals up to saturation, were detailed. Experimental observations suggested that once the moisture diffuses into the bulk adhesive and even before full saturation, a reduction of approximately 20% is expected for the modulus and the strength. Afterwards, the effect of ageing on the bulk adhesive is less significant than the experimental scatter in a single batch being tested.

- Moisture uptake

The water uptake into the bulk adhesive was studied using three different methodologies a) Gravimetric analysis b) Electrochemical Impedance Spectroscopy and C) ATR-FTIR. Furthermore, both the effect of temperature and the effect of ions were investigated. In most cases, the results obtained from different methods were in agreement with each other and the diffusion coefficient at room temperature for marine environment (3.5% NaCl) was found to be around $(3.3 \pm 0.25)*10^{-13}$ m^2s^{-1}. There was no significant difference in the kinetics of water uptake between electrolyte and deionized water. At room temperature, the water uptake followed typical Fickian behavior. The maximal absorption was found to be around 1.9% for salt water and 2.5% for deionized water at room temperature. With increase in temperature, the kinetics of water uptake increased which is also reflected in the values obtained for diffusion coefficient. It was also observed that at high temperatures, the sorption behavior was anomalous and didn't follow typical Fickian behavior. Weight loss was observed due to resin peeling and/or leaching.

- Mode I fracture toughness

Using DCB testing, the energy release rate for the steel-adhesive interface was determined in mode I. This was done for non-aged specimens as well as 6 weeks-aged specimens. The reported energy release rate did not show significant difference due to the 6 weeks of ageing with a mean value of approximately 1.1 kJ/m^2. The use of DIC enabled further understanding of the crack propagation phenomenon via studying the fracture process zone ahead of the crack tip and the strain contour maps during the test. Further analysis of the fractured surfaces revealed that the failure differed at the center of all specimens compared to the edges. This was attributed to the stress state nature change across the width from plane stress to plane strain conditions.

- Mode II fracture toughness

An experimental study on the fracture of MMA adhesive under mode II is reported. The TAST specimen geometry was used for the evaluation of the interfacial fracture toughness under mode II. Utilizing the TAST specimen, the effect of the adhesive layer thickness on the shear strength and the maximum shear strain across the adhesive layer was investigated. Moreover, the effect of the pre-crack length on the shear strength of the joints was presented. The adhesive layer experienced large shear strain deformations of 0.18 to 0.35 (depending on the adhesive layer thickness) before damage propagation. The pre-crack length did not show to have a strong effect on the magnitude of the shear deformations. For the first 5 to 15 mm, the crack propagated slowly while the load was slightly increasing. After the peak load was reached however, the crack started to grow more rapidly. The Mode II MMA/steel interfacial fracture toughness (G_{IIC}) is found to be $4.2 \pm 0.5\ kJ/m^2$ for the non-aged case and $1.8 \pm 0.3\ kJ/m^2$ for the aged case (80 °C, full immersion in salt-water, 3.5 % salinity).

- Delamination crack-growth

Scanning Kelvin probe study was performed to understand the delamination mechanism from the vicinity of an artificial defect. The samples were prepared with an artificial defect where an electrolyte reservoir was created and placed in 93% humidity after which the potential distribution under buried interfaces were probed to understand the delamination behavior. S curves which are typical of cathodic delamination were obtained. The rate of delamination, calculated by tracking the lateral deflection of the inflection point in S curve, was found to be 153 ± 6 µm/min$^{1/2}$.

5. REFERENCES

[1] Broughton W. Testing the mechanical, thermal and chemical properties of adhesives for marine environments. Adhes. Mar. Eng., 2012, p. 99–154. doi:10.1533/9780857096159.2.99.

[2] van Westing EPM, Ferrari GM, de Wit JHW. The determination of coating performance with impedance measurements—II. Water uptake of coatings. Corros Sci 1994;36:957–77. doi:https://doi.org/10.1016/0010-938X(94)90197-X.

[3] Saleh MN, Saeedifar M, Zarouchas D, De Freitas ST. Stress analysis of double-lap bi-material joints bonded with thick adhesive. Int J Adhes Adhes 2019:102480. doi:10.1016/J.IJADHADH.2019.102480.

[4] Heshmati M, Haghani R, Al-Emrani M. Durability of bonded FRP-to-steel jointsEffects of moisture, de-icing salt solution, temperature and FRP type. Compos Part B Eng 2017;119:153–67. doi:10.1016/j.compositesb.2017.03.049.

[5] ASTM D5528-01: Standard test method for mode I interlaminar fracture toughness of unidirectional fiber-reinforced polymer matrix composites. Am Stand Test Methods 2014;03:1–12. doi:10.1520/D5528-13.2.

[6] Dean G, Crocker L, Read B, Wright L. Prediction of deformation and failure of rubber-toughened adhesive joints. Int J Adhes Adhes 2004;24:295–306. doi:https://doi.org/10.1016/j.ijadhadh.2003.08.002.

[7] Karachalios EF, Adams RD, da Silva LFM. Single lap joints loaded in tension with high strength steel adherends. Int J Adhes Adhes 2013;43:81–95. doi:https://doi.org/10.1016/j.ijadhadh.2013.01.016.

[8] Kosmann J, Klapp O, Holzhüter D, Schollerer MJ, Fiedler A, Nagel C, et al. Measurement of epoxy film adhesive properties in torsion and tension using tubular butt joints. Int J Adhes Adhes 2018;83:50–8. doi:https://doi.org/10.1016/j.ijadhadh.2018.02.020.

[9] Walrath DE, Adams DF. The losipescu shear test as applied to composite materials. Exp Mech 1983;23:105–10. doi:10.1007/BF02328688.

[10] Yen S-C, Craddock JN, Teh KT. Evaluation of a modified Arcan fixture for the in-plane shear test of materials. Exp Tech 1988;12:22–5. doi:10.1111/j.1747-1567.1988.tb02169.x.

[11] Adams RD, Adams RD, Comyn J, Wake WC, Wake WC. Structural Adhesive Joints in Engineering. Springer; 1997.

[12] ASTM-D5656-04. Standard Test Method for Thick-Adherend Metal Lap-Shear Joints for Determination of the Stress-Strain Behavior of Adhesives in Shear by Tension

Loading. Annu B ASTM Stand 2004;10:1–8. doi:10.1520/D5656-10R17.2.

[13] Sababi M, Terryn H, Mol JMC. The influence of a Zr-based conversion treatment on interfacial bonding strength and stability of epoxy coated carbon steel. Prog Org Coatings 2017;105:29–36. doi:https://doi.org/10.1016/j.porgcoat.2016.11.016.

[14] ASTM B117: Standard Practice for Operating Salt Spray (Fog). ASTM Stand 2011:1–12. doi:10.1520/B0117-11.2.

[15] Saeedifar M, Saleh MN, De Freitas ST, Zarouchas D. Damage characterization of adhesively-bonded Bi-material joints using acoustic emission. Compos Part B Eng 2019;176. doi:10.1016/j.compositesb.2019.107356.

[16] Krieger RB, for the Advancement of Material S, Engineering P. Stiffness Characteristics for Structural Adhesives for Stress Analysis in Hostile Environment. Society for the Advancement of Material and Process Engineering; 1975.

[17] Kassapoglou C, Adelmann JC. KGR-1 thick adherend specimen evaluation for the determination of adhesive mechanical properties. SAMPE Q 1992;24:19–27.

[18] Chauffaille S, Devos O, Jumel J, Shanahan MER. Liquid diffusion in polymeric adhesives by electrochemical-impedance spectroscopy (EIS). Int J Adhes Adhes 2010;30:602–8. doi:https://doi.org/10.1016/j.ijadhadh.2010.05.010.

[19] Zhou J, Lucas JP. The effects of a water environment on anomalous absorption behavior in graphite/epoxy composites. Compos Sci Technol 1995;53:57–64. doi:https://doi.org/10.1016/0266-3538(94)00078-6.

[20] Miszczyk A, Darowicki K. Water uptake in protective organic coatings and its reflection in measured coating impedance. Prog Org Coatings 2018;124:296–302. doi:https://doi.org/10.1016/j.porgcoat.2018.03.002.

[21] Vlasak R, Klueppel I, Grundmeier G. Combined EIS and FTIR–ATR study of water uptake and diffusion in polymer films on semiconducting electrodes. Electrochim Acta 2007;52:8075–80. doi:https://doi.org/10.1016/j.electacta.2007.07.003.

[22] Bordes M, Davies P, Cognard J-Y, Sohier L, Sauvant-Moynot V, Galy J. Prediction of long term strength of adhesively bonded steel/epoxy joints in sea water. Int J Adhes Adhes 2009;29:595–608. doi:https://doi.org/10.1016/j.ijadhadh.2009.02.013.

[23] Nguyen Dang D, Peraudeau B, Cohendoz S, Mallarino S, Feaugas X, Touzain S. Effect of mechanical stresses on epoxy coating ageing approached by Electrochemical Impedance Spectroscopy measurements. Electrochim Acta 2014;124:80–9. doi:https://doi.org/10.1016/j.electacta.2013.08.111.

[24] Tao R, Li X, Yudhanto A, Alfano M, Lubineau G. On controlling interfacial heterogeneity to trigger bridging in secondary bonded composite joints: An efficient strategy to introduce crack-arrest features. Compos Sci Technol 2020;188:107964. doi:10.1016/j.compscitech.2019.107964.

[25] Persson BNJ. Fracture of polymers. Phys. Deform. Fract. Polym., Cambridge University Press; 2013, p. 391–434. doi:10.1063/1.478936.

[26] Wylde JW, Spelt JK. Measurement of adhesive joint fracture properties as a function of environmental degradation. Int J Adhes Adhes 1998;18:237–46. doi:https://doi.org/10.1016/S0143-7496(98)00028-1.

[27] Loh WK, Crocombe AD, Wahab MMA, Ashcroft IA. Environmental degradation of the interfacial fracture energy in an adhesively bonded joint. Eng Fract Mech 2002;69:2113–28. doi:https://doi.org/10.1016/S0013-7944(02)00004-8.

[28] Liljedahl CDM, Crocombe AD, Wahab MA, Ashcroft IA. Modelling the environmental degradation of adhesively bonded aluminium and composite joints using a CZM approach. Int J Adhes Adhes 2007;27:505–18. doi:https://doi.org/10.1016/j.ijadhadh.2006.09.015.

[29] Ameli A, Papini M, Spelt JK. Hygrothermal degradation of two rubber-toughened epoxy adhesives: Application of open-faced fracture tests. Int J Adhes Adhes 2011;31:9–19. doi:https://doi.org/10.1016/j.ijadhadh.2010.10.001.

[30] Heshmati M, Haghani R, Al-Emrani M. Dependency of cohesive laws of a structural adhesive in Mode-I and Mode-II loading on moisture, freeze-thaw cycling, and their synergy. Mater Des 2017;122:433–47. doi:https://doi.org/10.1016/j.matdes.2017.03.016.

[31] Kinloch AJ, Lau CC, Williams JG. The peeling of flexible laminates. Int J Fract 1994;66:45–70. doi:10.1007/BF00012635.

APPENDIX

Effect of Temperature on Mechanical Properties of Adhesives

Tensile Tests

Tensile tests were performed on dog-bone specimens using a strain rate of $3 \times 10^{-4}\ s^{-1}$in -40 C, room temperature, and +80 C. The results are summarized in Fig. 47 and 48.

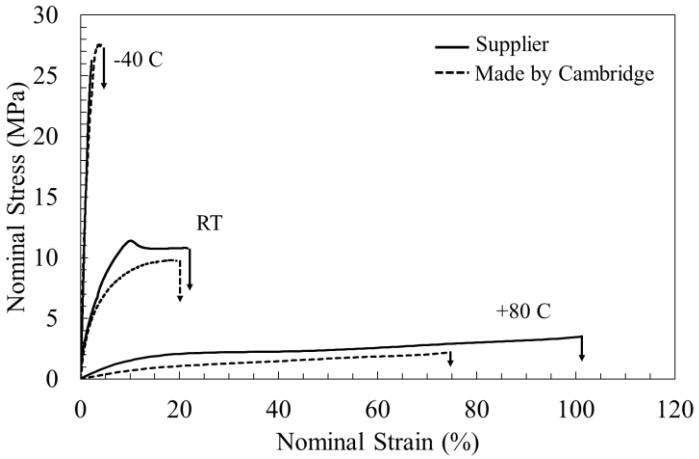

Figure 47: Nominal stress-strain curves obtained from tensile tests performed at different temperatures. The difference between specimens fabricated by University of Cambridge and the ones provided by the supplier is investigated.

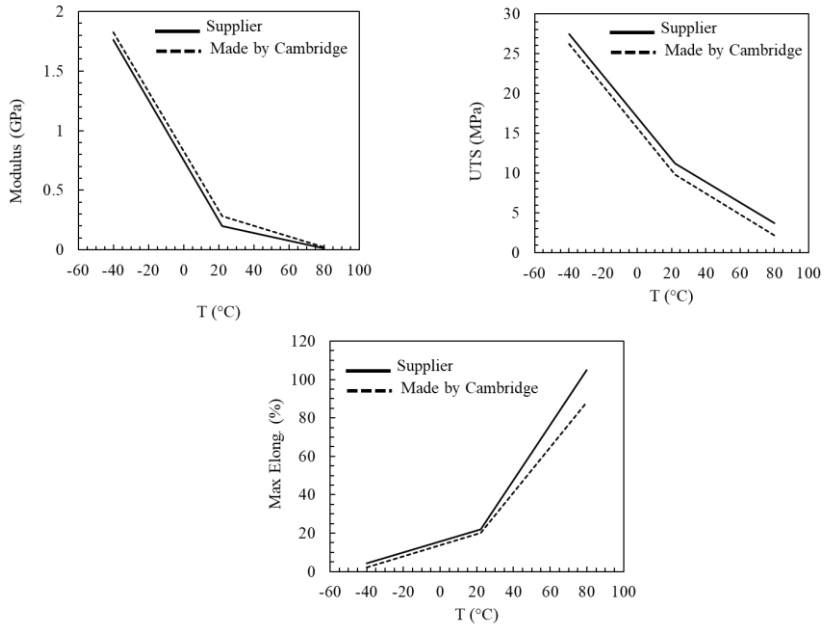

Figure 48: Effect of temperature on the tensile elastic modulus, ultimate strength and elongation at break of MMA -300.

Table 4 Effect of temperature on MMA-300 properties

	Elastic modulus (MPa)	Strength (MPa)	Max elongation (%)
-40 C	1805 ± 124	26.3 ± 0.9	3 ± 1
RT	245 ± 23	10.5 ± 0.5	26 ± 12
+80 C	22 ± 5	2.9 ± 0.4	92 ± 7

DMA

Dynamic Mechanical Analysis (DMA) for two different frequencies and for a range of temperatures (-60 to 80 °C) is performed. A typical result is presented in Fig. 49.

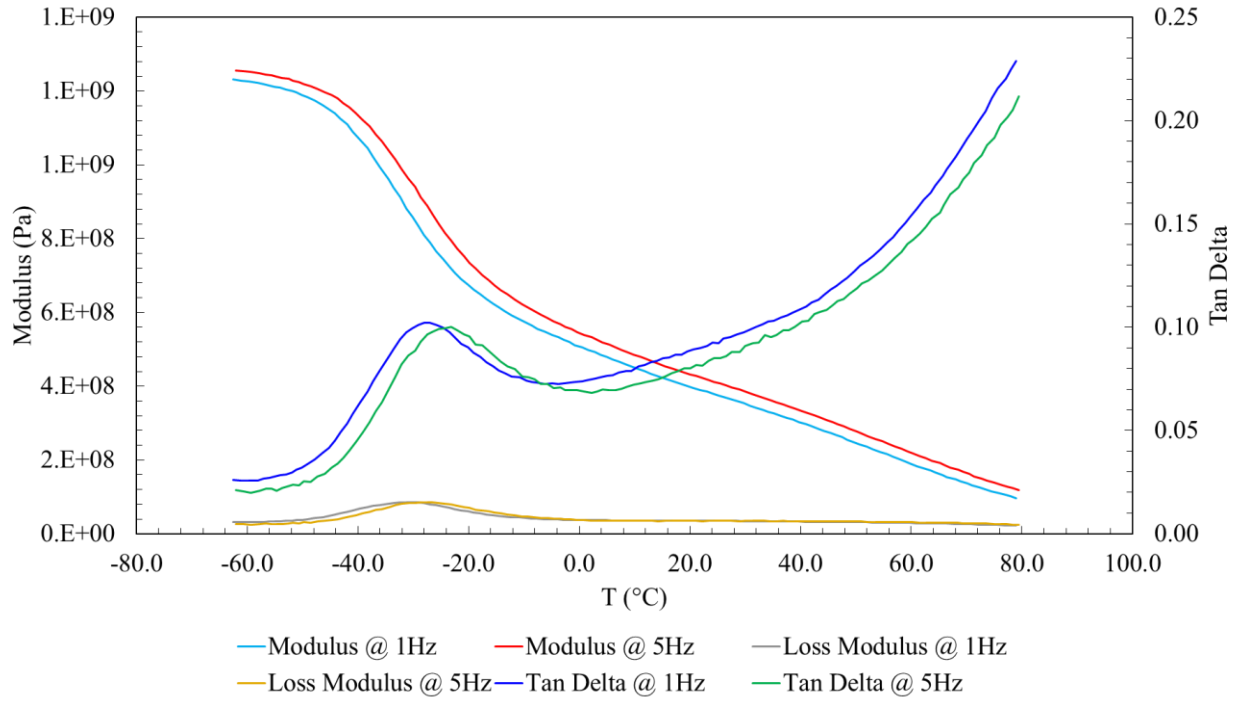

Figure 49: DMA results performed on MMA-300 specimen.

Mode I Fracture Toughness (90° peel test)

Introduction

Extracting cohesive laws after a given exposure time is a non-trivial objective and a complicated combined experimental and numerical methodology is required. A common approach is to use DCB/ENF specimens and test them after exposure to given conditions. However, the limitation of this methodology is that it is sensitive to the geometry and the size of the specimens. Smaller specimens are affected more since moisture ingress affects a larger part of the joint while larger joints are affected less. In addition, in this classic approach, the damage in the adhesive layer is non-uniform, as the moisture enters the joint from the sides and gradually moves to the center. Therefore, different areas of the adhesive layer experience different moisture concentrations. As a result, a single cohesive law cannot be obtained.

This limitation can be tackled by utilizing open-face specimens as the ones shown in Fig. 50. Such configurations have been used extensively in the past [26–30] and have provided an effective way to measure interfacial properties after exposure. In this case, moisture diffuses through the thickness of the adhesive layer and therefore the damage in the substrate/adhesive interface is uniform. Such a configuration can be used for the classic DCB/ENF tests. In this case, after the exposure takes place, the second substrates are also bonded to the specimens and the classic DCB/ENF configuration is achieved. During, the test, the damage initiates at the damaged adhesive/substrate interface since this side has significantly reduced interfacial strength due to the exposure. A simplified approach of the open-face DCB specimen can be a 90° peel test which can offer a quick evaluation for the fracture toughness and does not require bonding a second substrate.

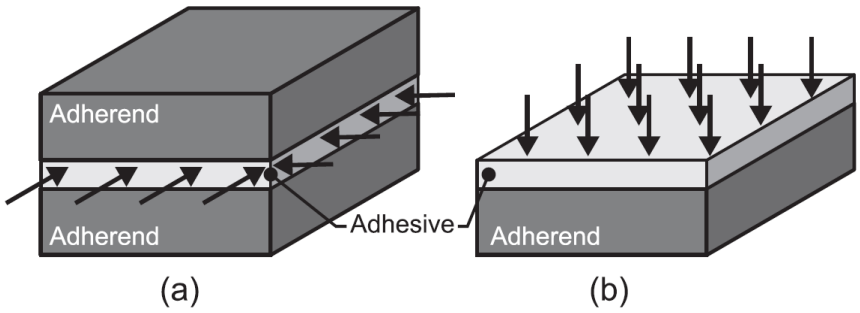

Figure 50: (a) Classic closed joint configuration, (b) open-face specimen configuration

Another advantage of the open-face specimen approach is that the degradation of the interfacial strength can be correlated to the time of exposure as well as with the concentration of moisture. The specimens can be tested after different exposure periods and this can lead to a correlation of the fracture toughness with time. In addition, the time can be correlated to the concentration of moisture considering the diffusion coefficient of the adhesive and the thickness of the adhesive layer. Therefore, a correlation between the fracture toughness and the concentration can also be established. This correlation will allow to create a multi-physics numerical approach where the cohesive properties are moisture-concentration dependent. Fig. 51 shows the combined numerical and experimental data that lead to the correlation of the fracture toughness.

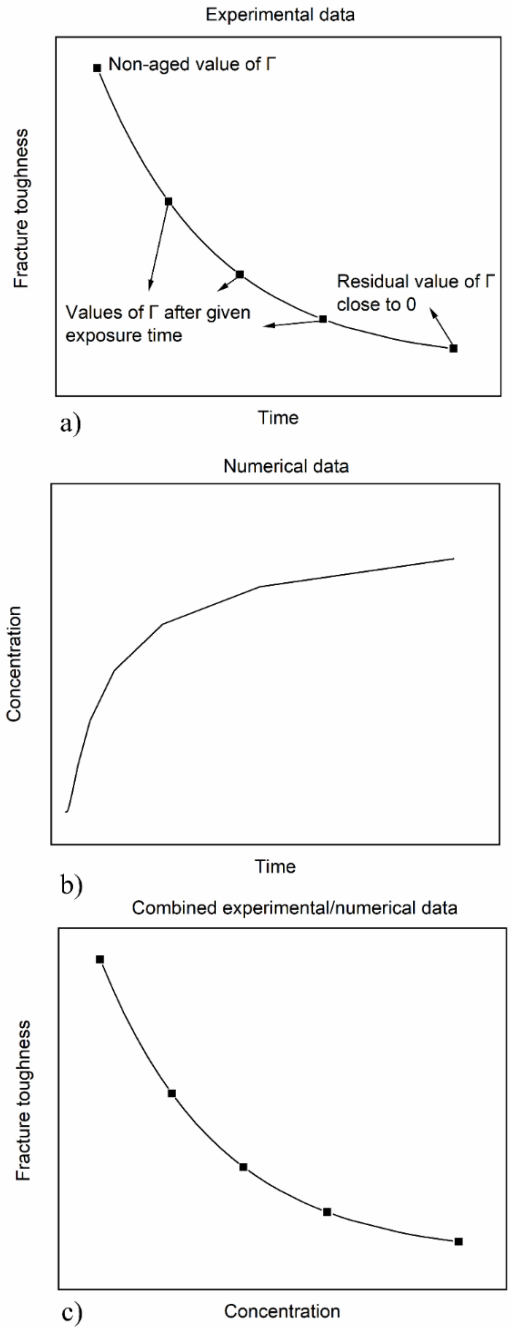

Figure 51: (a) Experimental correlation of time with fracture toughness, (b) numerical correlation of time with concentration, (c) combined experimental/numerical correlation of fracture toughness with concentration.

Experiments

The geometry of the peel specimens manufactured and tested is shown in Figure 52. The width of the specimen was 25 mm, the thickness of the adhesive layer was 0.85 mm and the thickness of the steel substrate was 3 mm. The thickness of the specimens was controlled with spacers and the specimens cured at ambient conditions and post-cured at 80°C for 1 hour. Afterwards, the specimens were immersed in salt-water (3.5% salinity) at 80°C and were removed gradually from the oven so that the effect of different exposure periods (and

hence salt-water concentrations) could be evaluated. It is worth noting that reinforcement was added on the back side of the specimen to avoid premature adhesive failures. Different types of reinforcements were used which yielded similar results.

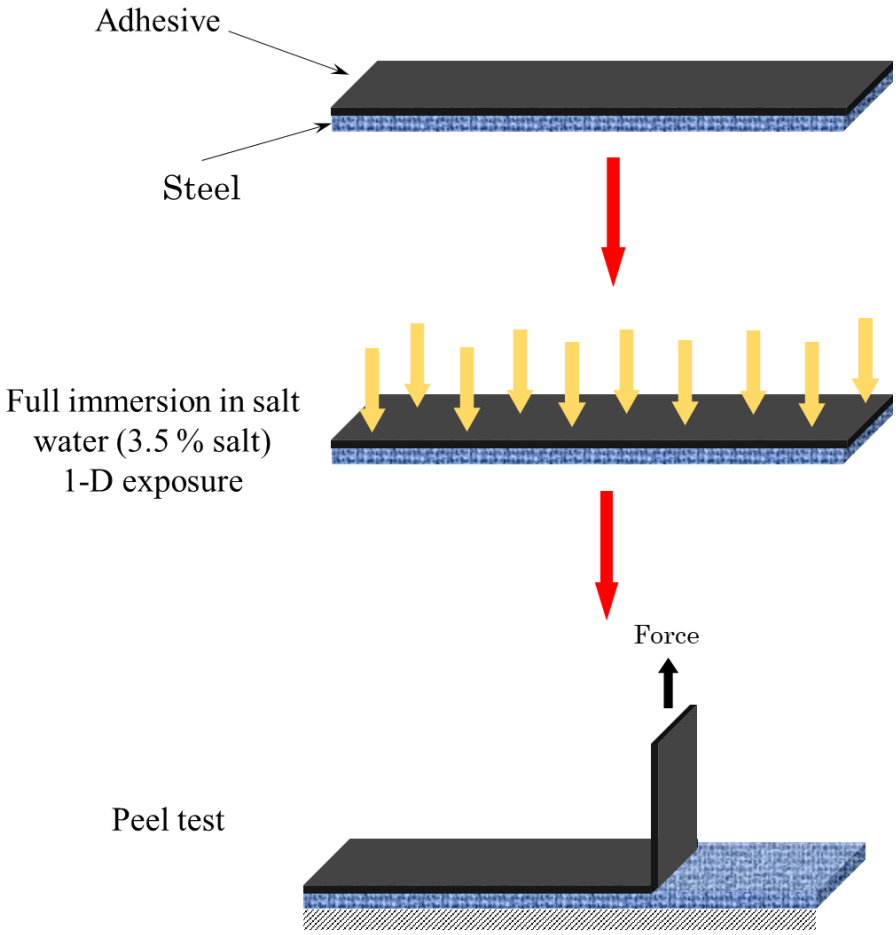

Figure 52: Sketch of the 90° peel test specimen, the exposure mechanism and the mechanical testing.

The load-displacement response of the specimens was recorded, and the peel load was used in order to calculate the interfacial fracture toughness. In addition, a camera was used to record the crack propagation as the test was progressing. The rate of loading during the test was 1 mm/min.

In general, in order to measure the interfacial fracture toughness of adhesive and a substrate through a peel test, a global energy analysis is needed. The input energy which is the work done on the adhesive layer, transforms to at least four types of energies: 1) elastic energy, 2) plastic energy, 3) bending energy and 4) the interfacial fracture energy. Hence, we can write:

$$\frac{dU_{ext}}{b \times da} = G_{int} + \frac{dU_s}{b \times da} + \frac{dU_p}{b \times da} + \frac{dU_{db}}{b \times da} \quad (1)$$

In equation (1), G_{int} is the interfacial toughness and *U* is energy with subscripts *ext*, *s*, *p*, and

db referring to external work, strain energy, dissipated tensile energy, and dissipated bending energy, respectively. The width of the specimen is *b* while *da* is the peel fracture length. Previous studies have shown that the elastic energy is negligible [31]. During the peel tests, the level of stresses is significantly lower than the adhesive yielding strength, the effect of plastic energy can be neglected as well. Hence, the adhesive interfacial toughness can be written as:

$$G_{int} = \frac{P}{b}(1 - \cos\theta) \quad (2)$$

In equation (2), θ is the peel angle. During the tests, the peel angle was kept close to 90° . The force-displacement curve to initiate and propagate a 10 mm peel fracture was recorded. The peel force is then obtained from the average force during the peel fracture.

Results

The peel specimens were evaluated after 4, 5 and 6 days in order to correlate the moisture concentration to the fracture toughness. The amount of moisture concentration was extracted numerically by considering the thickness of the adhesive layer and the diffusion coefficient. Fig. 53 shows characteristic load-displacement curves after 4 days of exposure. In addition, Fig. 53 also shows the gradual delamination of the adhesive/steel interface. In addition, Figure 54 shows the load-displacement curves after 4, 5 and 6 days and the gradual reduction of the average peel load with increasing time can be observed. Finally, Table 6 summarizes the results of the peel tests and correlates the moisture concentration with the interfacial fracture toughness.

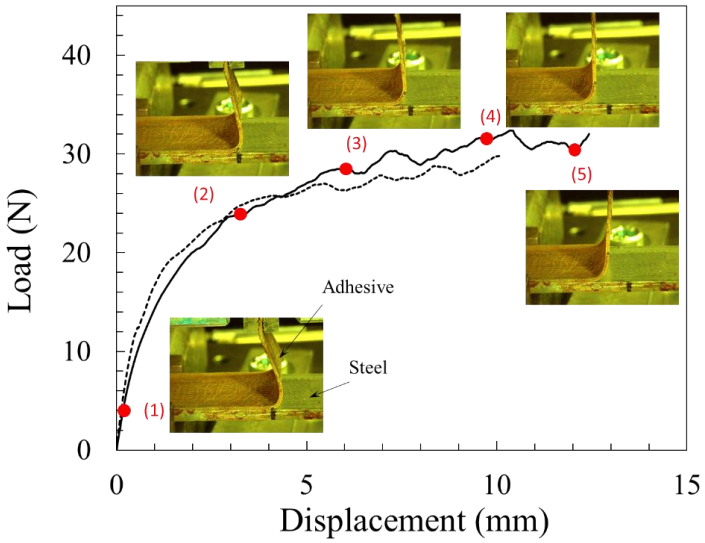

Figure 53: A typical load displacement curve obtained from peel test.

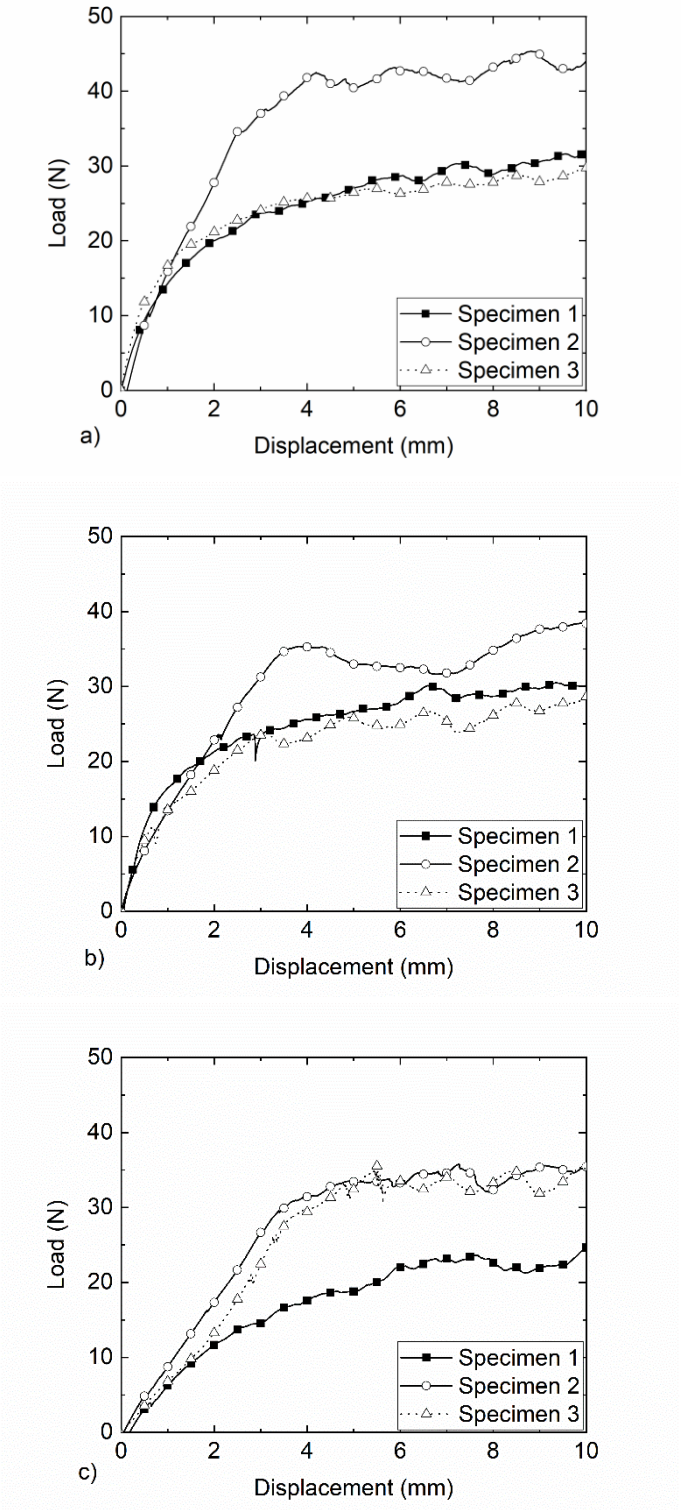

Figure 54: Load-displacement curves for the peel test after a) 4 days, 5) days and 6) days of exposure.

Table 5: Fracture toughness correlation with time of exposure and salt-water concentration

Time (Days)	Concentration (%)	Fracture toughness (kJ/m^2)
4	89	1.54
5	93	1.29
6	96	1.18

Conclusion

The peel test improves the understanding of the mechanism of the degradation of the interfacial fracture toughness since the damage introduced in the interface was uniform, and the evaluation took place over different exposure periods (and hence moisture concentrations). Initial results show the gradually increasing degrading effect of the salt-water in the steel/adhesive interface. However, the test needs to be repeated for more exposure periods before high fidelity predictions can be made.